



SAPIENZA  
UNIVERSITÀ DI ROMA

## PAPRICA: an innovative device for prompt-gamma detection in particle therapy applications

Facoltà di Scienze Matematiche Fisiche e Naturali  
Corso di Laurea Magistrale in Particles and Astroparticles

Candidate

Ilaria Avanzolini  
ID number 1650474

Thesis Advisor

Dott. Giacomo Traini

Co-Advisor

Dott. Marco Toppi

Academic Year 2019/2020

Thesis not yet defended

---

**PAPRICA: an innovative device for prompt-gamma detection in particle therapy applications**

Master's thesis. Sapienza – University of Rome

© 2020 Ilaria Avanzolini. All rights reserved

This thesis has been typeset by L<sup>A</sup>T<sub>E</sub>X and the Sapthesis class.

Author's email: [avanzolini.1650474@studenti.uniroma1.it](mailto:avanzolini.1650474@studenti.uniroma1.it)

# Contents

<b>Introduction</b>	<b>1</b>
<b>1 Particle Therapy</b>	<b>3</b>
1.1 Charged particles energy loss . . . . .	4
1.1.1 Bethe-Block and stopping power . . . . .	4
1.1.2 Range . . . . .	5
1.1.3 Multiple Coulomb Scattering . . . . .	6
1.1.4 Nuclear Fragmentation . . . . .	7
1.1.5 Dose and LET . . . . .	9
1.1.6 Bragg Peak . . . . .	10
1.2 Biological effects . . . . .	11
1.2.1 DNA damage . . . . .	11
1.2.2 Cell survival curves and RBE definition . . . . .	12
1.2.3 Oxygenation state dependence: OER . . . . .	14
1.3 Treatment administration . . . . .	15
<b>2 Range Monitoring techniques</b>	<b>17</b>
2.1 Range uncertainties sources . . . . .	17
2.2 Annihilation Gamma detection . . . . .	18
2.3 Monitoring exploiting charged particles detection . . . . .	20
2.4 Prompt Gamma . . . . .	21
2.4.1 Imaging system . . . . .	23
2.4.2 Non-imaging systems . . . . .	25
<b>3 The PAPRICA project</b>	<b>28</b>
3.1 Pair Production in PAPRICA . . . . .	28
3.2 The PAPRICA detector . . . . .	31
3.2.1 Converter . . . . .	32
3.2.2 Tracker . . . . .	32
3.2.3 Calorimeter . . . . .	33
3.2.4 Converter/Calorimeter read-out . . . . .	33
<b>4 Trigger and event selection</b>	<b>36</b>
4.1 FLUKA code . . . . .	36
4.1.1 PAPRICA simulation . . . . .	37
4.2 Trigger strategies and background analysis . . . . .	38
4.2.1 Study of the event topology . . . . .	38
4.2.2 Trigger using calorimeter in coincidence with converter . . . . .	41
4.2.3 Trigger using calorimeter information . . . . .	48
4.3 Expected trigger rate in a realistic scenario . . . . .	49

<b>5 Reconstruction of the prompt-gamma emission profile</b>	<b>51</b>
5.1 Reconstruction algorithm . . . . .	51
5.1.1 Photon direction . . . . .	51
5.1.2 Track identification and selection . . . . .	51
5.1.3 Lepton kinetic energy . . . . .	53
5.1.4 Vertex . . . . .	54
5.1.5 Photon emission point . . . . .	56
5.2 Results . . . . .	57
5.2.1 Photon angular resolution . . . . .	58
5.2.2 Impact of energy measurement on spatial resolution . . . . .	60
5.2.3 Systematic error . . . . .	62
5.3 Unfolding: a preliminary study . . . . .	63
5.3.1 Unfolding matrix . . . . .	63
5.3.2 Bragg peak calibration . . . . .	64
<b>Conclusions</b>	<b>68</b>
<b>Bibliography</b>	<b>70</b>

# Introduction

According to the World Health Organisation (WHO), cancer is the second cause of death in the world [1]. Radiotherapy together with surgery, it is one of the most effective techniques for treating different types of tumors. The goal of radiotherapy is to ~~destroy~~ cancerous tissues using ionizing particles, trying to preserve the surrounding healthy tissues.

Particle Therapy (PT) is an innovative radiotherapy technique for cancer treatment in which the dose is delivered by charged particles (protons or carbon ions). The use of charged particles beams in radiotherapy was at first considered in 1946 by Robert R. Wilson, which proposed to exploit the advantageous depth-dose curve of proton beams for cancer treatment [2]. Subsequently, around 1954 at the Lawrence Berkeley Laboratory (LBL) the first treatments on patients took place, initially with proton beams and later with helium ion beams [3]. Today PT is a widely used technique: more than 70 centers for proton and carbon ions therapy are currently in operation [4]. In Italy CNAO (*Centro Nazionale di Adroterapia Oncologica*, Pavia) has been operating since 2012 and it is one of the few centers (six worldwide) where both carbon ions and proton beams can be used. In Italy there are other two centers that treat patients with charged particles such as CATANA (*Centro di Adroterapia ed Applicazioni Nucleari Avanzate*) in Catania and the proton therapy center in Trento.

The development of PT has been driven by the search for a technique that minimizes the radiation delivered to healthy tissues during the cancer treatment. The energy release mechanism of charged particles is governed by the interactions of the beam particles with the atoms, resulting in the well known Bragg Peak (BP) distribution: as the particle slows down, the energy release increases, showing a peak near the particle stopping position. By changing the particle energy, it is possible to change the BP extension and treat the whole target volume. With respect to conventional radiotherapy, PT is clearly more suitable to treat tumors near organs at risk and pediatric patients in order to reduce significantly the dose released to the healthy tissues surrounding the tumour.

The high intrinsic spatial selectivity of the energy release in PT requires high accuracy in predicting the particle range. However several factors may lead to a wrong range estimation in the treatment planning phase, resulting in a shift of the Bragg peak position and in a wrong dosage of the tumour volume 

Since in PT the capability to deliver the dose at a certain depth depends on the capability to predict the beam range in the patient, the scientific community have addressed several researches to develop on-line beam range verification techniques. Until now there are not systems used in clinical practice that are able to monitor the range online. In PT the beam particles does not escape from the patient, and the main approach consists of an indirect range measurement, exploiting the secondary particles produced due to the nuclear interaction between the beam projectiles and the crossed tissues nuclei. This radiation is correlated in energy, space and time

with the primary beam range.

The PAPRICA project, started in 2019 and funded by Istituto Nazionale di Fisica Nucleare (INFN), proposes an innovative technique for range monitoring, exploiting the prompt-gamma detection ~~by~~ pair production mechanism. In this thesis the feasibility of such technique ~~will be~~ studied, evaluating the capability of detecting range variations ~~using~~ using the PAPRICA detector prototype ~~by~~ means of Monte Carlo simulations.

In chapter 1 the PT physical and biological aspects are described with a brief mention ~~on~~ treatment planning and facilities.

In chapter 2 the main range monitoring techniques that exploit prompt-gamma detection are described, focusing on their advantages and limitations.

In chapter 3 the design of the PAPRICA chamber prototype is described.

In chapter 4 the study of the main expected background sources, performed by means of a Monte Carlo simulation, is presented. The obtained results are used to chose and optimize the trigger logic as well as the criteria for the selection of the events of interest.

In chapter 5 the ~~performance of the gamma momentum reconstruction is shown~~ and its ~~implications in the range monitoring performance is discussed~~.

# Chapter 1

## Particle Therapy

Radiotherapy with electron beams and X-rays is a widely used technique for the treatment of cancer. The purpose of sending ionizing radiation treatments is to damage the DNA of cancer cells in order to prevent their replication and induce death. Electron beams (with energy of few MeV) are generally indicated for superficial tumors, due to their short range. Photon beams are instead used in the case of depth seated tumors, but they release a not negligible amount of energy even in healthy tissues located before and after the tumor mass. Trying to minimize these energy deposits is therefore crucial, as they can lead to serious side effects, that may occur months or years after the therapy administration, including a large set of diseases depending on the cancer type, i.e. fibrosis, infertility or a second cancer caused by radiation exposure.

The physical dose ( $D$ ) is defined as the average energy  $dE$  deposited by the radiation in an element of mass  $dm$ , as in Equation 1.1:

$$D = \frac{dE}{dm} \quad [1GY = 1J/Kg] \quad (1.1)$$

The dose is the physical quantity ~~that measures the delivered radiation~~, it is used to quantify the radiation effects ~~as it is connected to the biological damage level induced to the cells~~.

Particle Therapy (also called Hadrontherapy or ion-therapy) is an alternative type of radiation therapy in which accelerated light ion beams, mainly protons or  $^{12}C$  ions, in the energy range of 50-250 MeV (protons) and 150-400 MeV/u ( $^{12}C$  ions), are used instead of photons. The main advantage ~~leads~~ by charged ions is due to their characteristic energy loss curve: most of the energy released by a charged particle is located at the end of the particle path, in a few mm wide region called Bragg Peak (subsection 1.1.6). Combining hadron beams at different energies, it is possible to build treatment plans in which the undesired dose to healthy tissues results considerably lower than what is possible to achieve in conventional radiotherapy. Moreover, the different processes involved in the energy loss in PT lead to a higher biological damage to the cells, especially for  $^{12}C$  ions treatments, making the PT recommended for radio-resistant tumours treatment.

In this chapter the physics principles of PT are summarized. Firstly the interactions of charged particles with matter and their effects on biological tissues are described. Finally a review of PT facilities and treatment modalities will be presented in the last section.

## 1.1 Charged particles energy loss

Charged hadrons interact with matter through electromagnetic and strong interactions, yielding their kinetic energy. The electromagnetic interaction with the electrons generally causes loss by ionization and loss of energy for Bremsstrahlung, but in the energy ranges typically used in hadrontherapy the latter is negligible. The strong interaction, on the other hand, causes fragmentation of the projectile or the target nuclei.

### 1.1.1 Bethe-Block and stopping power

The main processes responsible for the energy loss of the charged particles of the therapeutic beams are the inelastic collisions of the nuclei with the electrons of the atoms of the matter crossed. The ions interact with the electrons of the matter on which they affect by ionizing it.

The Bethe-Block formula [6], shown in Equation 1.2, describes the loss of energy per unit space traveled for a massive particle that loses energy by ionization in a material.

$$-\frac{dE}{dx} = 2\pi \frac{N_A Z \rho}{A} \frac{r_e^2 m_e c^2 z^2}{\beta^2} \left( \ln \frac{2m_e c^2 \beta^2 \gamma^2 W_{max}}{I^2} - 2\beta^2 - \delta(\gamma) - 2\frac{C}{Z} \right) \quad (1.2)$$

$W_{max}$  indicates the maximum energy that can be transferred in a collision and may be deduced from kinematic calculations as in Equation 1.3:

$$W_{max} = \frac{2m_e c^2 \beta^2 \gamma^2}{1 + \frac{2m_e}{M} \sqrt{1 + \beta^2 \gamma^2 + \frac{m_e^2}{M^2}}} \quad (1.3)$$

The mean excitation potential  $I$  is the average energy needed to excite an electron of the target material. It is a difficult quantity to analytically calculate and it is in general obtained by means of experimental measurements. The term  $\delta$  takes into account the effect of electron polarisation, that shields far electrons and reduces the energy loss. The parameter  $C$ , called shell correction, describes the variations of the energy loss when the incident particle speed is comparable or lower than the orbital speed of the bound electrons. The other physical quantities are shown in Table 1.1.

$N_A$	Avogadro's number
Z	Atomic number of absorbing material
A	Atomic weight of absorbing material
$\rho$	Density of absorbing material
$m_e$	$e^-$ mass
$r_e$	Classical $e^-$ radius
c	Light speed
z	Charge of projectile (in units of e)
$\beta$	v/c of projectile
$\gamma$	Lorentz factor
M	Mass of absorbing material

**Table 1.1.** Physical quantities present in Equation 1.2

For the energies of interest in PT ( $\beta\gamma < 2$ ) the function follows the  $\frac{1}{\beta^2}$  trend. During the process the incident particle slows down by decreasing  $\beta\gamma$  and thus

increasing  $\frac{dE}{dx}$  up to a maximum, after which the particle has lost all its energy. The average  $\frac{dE}{dx}$  represents the *stopping power*, that is the average energy lost by a particle per unit path. The Figure 1.1 shows the trend of stopping power due to ionization for different materials.

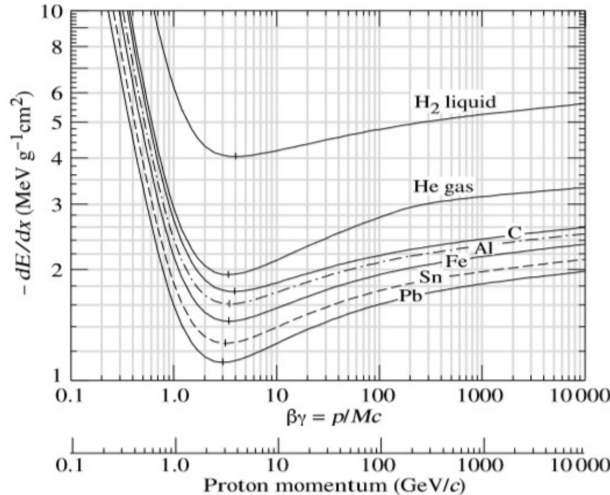


**Figure 1.1.** Trend of the energy loss by ionization (Bethe-Bloch formula) as a function of the  $\beta\gamma$  product of the particle for different materials [5]. The scale below shows the corresponding momentum value for protons.

The Bethe-Bloch equation refers to an average energy loss per length unit. In fact for a given charged particle the number of collisions with atomic electrons is affected by statistical fluctuation, as well as the energy lost in a single collision. As a consequence, the measured energy spectrum of a monochromatic charged particle beam after the passage through a layer of a given thickness is broaden, since the energy loss is different for each single particle. This is known as Energy straggling. For thick absorbers the number of collision is well described by a Gaussian distribution, since the Central limit theorem can be assumed. For thinner absorber more complicated models, proposed by Landau and Vavilov, are needed to predict the deposited energy distributions.

### 1.1.2 Range

The range is defined as the path that a particle can travel before losing all its kinetic energy. The theoretical range can be calculated from Equation 1.4:

$$R(E) = \int_0^E \left( \frac{dE'}{dx} \right)^{-1} dE' \quad (1.4)$$

This definition is very useful to give raw estimates of ranges using scale laws. For instance it is easy to see that, given a material, for two different ions having respectively masses  $M_1$ ,  $M_2$ , charges  $z_1$ ,  $z_2$ , and the same energy per nucleon the range scale follows the equation Equation 1.5:

$$\frac{R_1}{R_2} = \frac{M_1 z_2^2}{M_2 z_1^2} \quad (1.5)$$

The number of interactions and the energy release are not the same for each particle and change according to the individual trajectory. ~~The range can be therefore statistically described by a probability function.~~ This effect is known as *range straggling*. Therefore, once the initial energy is fixed, the range of a particle can assume different values and, for large thicknesses crossed, the range dispersion is described by a Gauss distribution, centered in the mean range  $R$  with a relative standard deviation equal to Equation 1.6:

$$\frac{\sigma_R}{R} = \frac{1}{\sqrt{M}} f \frac{E}{Mc^2} \quad (1.6)$$

where  $f$  is a function that varies slowly depending on the absorber,  $M$  and  $E$  are the mass and energy of the particle respectively.

The range can be experimentally estimated sending a mono-energetic beam on targets with different thicknesses and measuring the fraction of escaped particles for each target as a function of the thickness. In this way, a curve similar to what is shown in the Figure 1.2 is achieved.

Moreover from Figure 1.2 the *mean range* can be defined as the midpoint of the descent curve, i.e. the point where the particles transmitted fraction over the total is  $1/2$ . Although in many applications it is more interesting to know the thickness within which all the particles are absorbed. This thickness, called *extrapolated range*, can be obtained extrapolating the tangent to the curve at half height to zero.

An example of charged particles range in water as a function of the projectile energy is shown in Figure 1.3. Comparing proton and carbon ions the scale factor is  $\approx 3$ . For this reason ion therapy requires higher energy beam in order to reach deep targets.

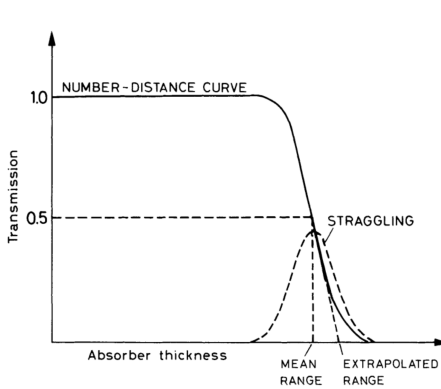


**Figure 1.2.** Typical curve showing the fraction of transmitted particles as a function of the target thickness [6].

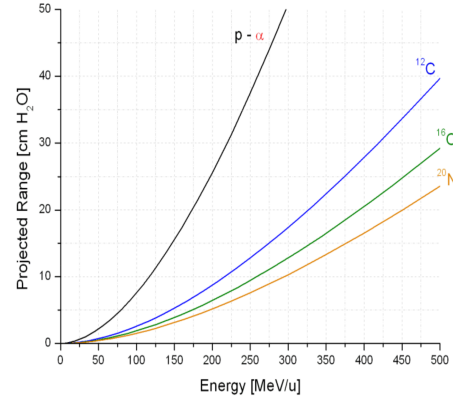


**Figure 1.3.** Charged particle range in water as a function of the initial energy, obtained with a Monte Carlo simulation [8]

### 1.1.3 Multiple Coulomb Scattering

Another important interaction that arises when a charged particle passes through the matter ~~is the Coulomb scattering with the target nuclei~~ whose main effect on a charged particle beam is the widening of the transverse beam distribution. The beam widening depends on the traversed thickness, the medium crossed, the properties of the particles and the beam energy. When the thickness is extremely small and the

probability to have more than one interaction is negligible, the effect is well described by the Rutherford formula with the differential cross section as in Equation 1.7.

$$-\frac{d\sigma}{d\Omega} = z^2 Z^2 r_e^2 \frac{m_e^2 c^2}{4\beta^2 p^2 \sin^4 \theta / 2} \quad (1.7)$$

where  $p$  stands for the momentum of the incoming particle and  $\theta$  is the deflection angle, while the other symbols have the same meaning as in Table 1.1.

When the thickness increases and the number of interactions becomes high, the angular dispersion with respect to the beam direction, can be described by a Gaussian distribution, centred in  $\theta=0$ , with root mean square as in Equation 1.8.

$$\sigma_{\theta_0} = \frac{13.6 MeV}{\beta cp} z \sqrt{\frac{x}{X_0}} \left[ 1 + 0.0038 \ln\left(\frac{x}{X_0}\right) \right] \quad (1.8)$$

where  $p$  is the momentum of the particle,  $x$  is the distance covered in the target, and  $X_0$  is the radiation length of the material.

Figure 1.4 shows the variation of the lateral spreading as a function of the penetration into the water for different particles, and it is immediately clear that for the same penetration depth the lateral spreading decreases as the mass of the incident particles increases (the dependence on the mass is due to the  $\beta p$  factor in Equation 1.8).

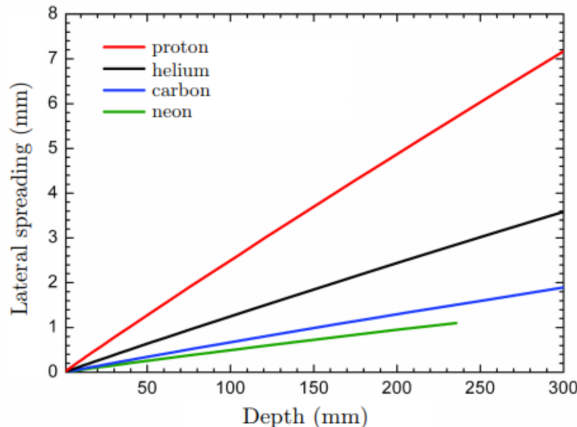


**Figure 1.4.** Lateral spreading in water for different particles as a function of penetration depth, obtained with Monte Carlo simulation. [9]

#### 1.1.4 Nuclear Fragmentation

In particle therapy the energy of protons and light ions may be sufficient to go beyond the Coulombian barrier, leading to a nuclear reaction between the projectile and the target nucleus.

The nuclear reactions between the beam and the target nuclei, at the energies of particle therapy, can be described using the abrasion-ablation model, represented in Figure 1.5.

In the first phase of this model (abrasion) a particle of the incident beam hits the target nucleus of the crossed material, light particles are then emitted and fragments of the target and projectile particles are formed. This phase is very rapid and the interaction occurs on a time scale of  $10^{-23}$  -  $10^{-21}$  s.

In the second phase (ablation) the remaining fragments of projectile and target are de-excited due to evaporation of neutrons, protons and light nuclei, fission and emission of gamma rays. The characteristic time of emission of particles varies from  $10^{-21}$  to  $10^{-16}$  s.

The high-energy fragmentation reactions that occur along the path of the beam inside the tissues lead to the attenuation of the initial flux of the beam and the accumulation of secondary low-charge fragments. These effects become more significant as the energy of the projectile particle increases and therefore, for a greater penetration depth of the initial beam.

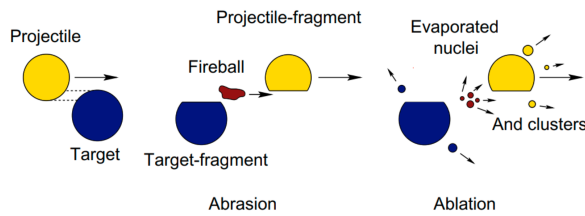


**Figure 1.5.** Abrasion-ablation model scheme [8]

The effects of the nuclear reactions just described are relevant in PT. The main consequences are:

- The decay products of unstable nuclei and secondary particles formed in the interaction processes can in some cases be exploited to obtain dosimetric information. This will be described in chapter 2.
- The dose distribution is modified. The projectile fragments, with lower atomic mass, have a comparable and in some cases higher range than the primary hadron (range  $\approx A/Z^2$ ). This results in an energy deposit at depths greater than the Bragg peak, generating a characteristic tail in the dose distribution (see Figure 1.6). The probability of fragmentation increases as the mass of hadron increases, therefore it is preferred to use light ions in PT treatments. For the proton beams only the fragmentation of the target occurs, the fragments have a range that does not exceed a few micrometers and the dose tail after the Bragg peak is almost negligible.
- The generated secondaries cause a lateral widening of the released dose distribution in addition to that due to multiple Coulomb scattering.

However, the occurrence of nuclear reactions does not change the position of the Bragg peak, which is defined only by the Bethe-Bloch formula.

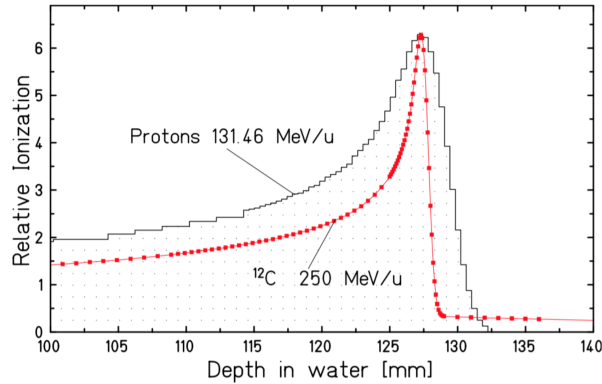


**Figure 1.6.** Dose released by a 131 MeV proton beam in water (black line), and by a  $^{12}C$  ion beam at 250 MeV/u (red line). The latter shows the characteristic dose tail beyond the Bragg peak due to the fragmentation [8].

### 1.1.5 Dose and LET

The dose deposited in the tissue is the most important physical quantity in radiotherapy, because it allows to link physical quantities to clinical effects. It has been defined at the beginning of this chapter (Equation 1.1) as the energy loss by ionising radiation per mass unit.

In the inelastic collisions of the nuclei with the electrons of the atoms of the crossed matter, the projectile with kinetic energy  $E_c$  loses an energy  $\delta E = e_c + I$  where  $e_c$  is the energy of the outgoing electron and  $I$  the ionization potential of the electron. Most of the electrons are stopped near their point of emission, while some of them have enough energy to move away and deposit their energy in a second region ( $\delta$  electrons).

Therefore the energy absorbed locally by the material  $E_{dep}$  is not exactly the same as the *stopping power*. LET (*Linear Energy Transfer*) is defined as the energy transferred from the beam to the material per unit of length (Equation 1.9):

$$LET = \left( \frac{dE}{dx} \right) - \sum E_c(e_\delta) \quad (1.9)$$

where  $\sum E_c(e_\delta)$  is the total kinetic energy of  $\delta$  electrons that have energy above a certain threshold. The LET therefore does not take into account the energy released by the  $\delta$  electrons produced within the volume under consideration. In most applications, however, the LET can be identified with the loss of energy:  $\frac{dE}{dx} \approx LET \approx \frac{E_{dep}}{dx}$ .

The dose can also be calculated as Equation 1.10:

$$D = \frac{dN}{dS} \frac{LET}{\rho} \quad (1.10)$$

where  $\frac{dN}{dS}$  is the beam fluence and  $\rho$  is the material density. Since the density of the medium is known and it is possible to calculate the fluence, it is necessary to know the LET of the beam particles in order to obtain the dose released.

### 1.1.6 Bragg Peak

The fundamental reason why particle therapy is preferable to the conventional radiotherapy with photons lies in the shape of charged particle depth-dose profile (Bragg curve) shown in Figure 1.7.

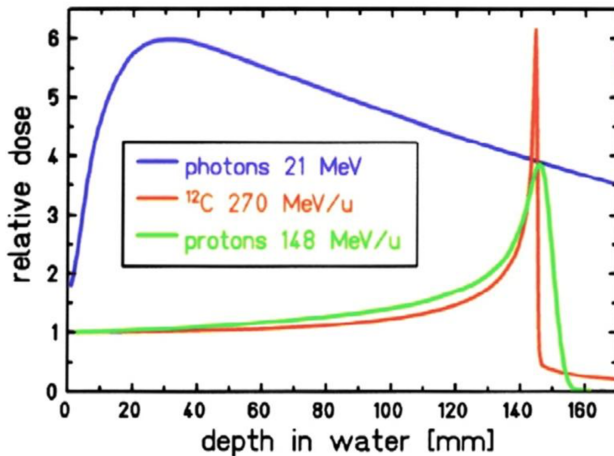


**Figure 1.7.** Dose profile in water of carbon ions of 270MeV/u, protons of 148MeV/u and highly energetic photons [7].

From Figure 1.7 it is observed that the photons present the maximum dose deposited at a depth of a few millimeters from the beginning of the interaction with the tissues and then show an exponential decrease with increasing depth.

In contrast, the dose profile of protons and heavy ions is characterized by a flat, low dose trend in the entrance channel, followed by a narrow peak, called the *Bragg peak*, at the end of their path. The depth of the Bragg peak can be precisely adjusted by changing the kinetic energy of the incident particles.

In Figure 1.7 is also observed that there is a weak dose release after the Bragg peak for carbon ions, due to fragmentation processes (as described in subsection 1.1.4). The probability of fragmentation increases as the mass of the hadron increases.

From Equation 1.2 it is described that the energy released by the charged particles depends on both the material crossed and the incident particle. It can therefore be understood why near the Bragg peak the LET of the carbon ions is greater than that of the protons. The loss of energy is in fact dominated by the term  $z^2$  which is greater for carbon ions.

The energy fluctuations that lead to the phenomenon of range straggling are the cause of the widening and lowering of the Bragg peak. Straggling is less for heavier particles, as it is inversely proportional to the mass of the particle itself (Equation 1.6).

The amplitude of the Bragg peak depends not only on the energy dispersion of the particle along the path, but also on the lateral dispersion of the beam. The lateral dispersion of the beam is less for heavy ions than for protons as described in subsection 1.1.3.

To cover the entire volume of the tumor, it is possible to combine beams with different energies. The resulting plateau (Figure 1.8) is called the Spread Out Bragg Peak (SOBP).

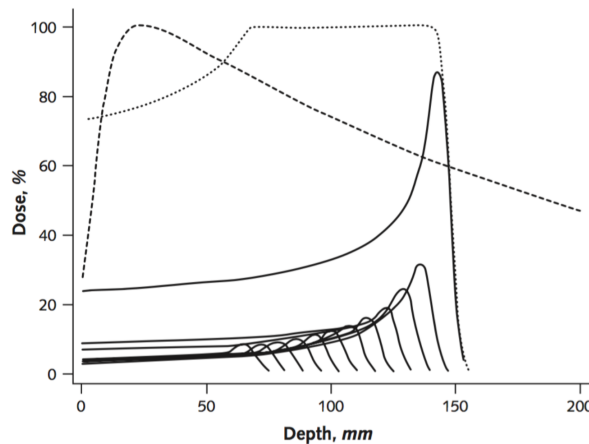


**Figure 1.8.** Bragg curves for beams of different energies (continuous line) and the spread-out Bragg peak (dotted line). The photon curve is also shown (dashed line) [10]

The well-defined range of charged particles in tissue with the final dose maximum followed by a sharp dose fall-off allows focusing the dose in the tumor while minimizing the damage of surrounding tissue. Therefore the high precision of particle therapy in spatial releasing the dose delivered to the patient makes it better compared to the conventional radiotherapy.

## 1.2 Biological effects

The effect of ionising radiations on biological tissues depends of several factors. The absorbed dose is not sufficient to properly quantify the amount of damages provoked to the cells, as tissues may have a different response to the exposure at different type of radiations. In this section the mechanisms underlying the radiation-induced cell damages are summarized, spotting the difference between PT and the standard radiotherapy.

### 1.2.1 DNA damage

When a ionizing radiation interacts with a biological tissue, the energy released by the particles induces chemical-biological effects that occur in subsequent times. The ionizing radiation may act on the DNA in a direct or indirect way. In both cases the result is to damage or change its structure. We speak of direct action when the primary radiation induces DNA damage by direct ionization of the DNA molecules. Instead, indirect action is defined when the DNA is damaged by free radicals, generated by the ionization of molecules present inside the cell, as in the case of the hydroxyl radical ( $OH^-$ ) which is generated when a water molecule absorbs radiation ( $H_2O \rightarrow OH^- + H^+$ ).

These actions lead to the formation of double or single DNA breaks. Double break is preferable as the damage is more difficult to repair. The probability to inflict a direct damage to the DNA cell depends on the LET and then on the charge of the incident particle ( $z^2$ ). High LET radiation will cause direct damage while low LET radiation will generate indirect damage.

An example of low-LET radiation is that of photons, while an example of high-LET radiation is that of carbon ions.

Figure 1.9 shows the average distance between ionization events for different values of the LET.

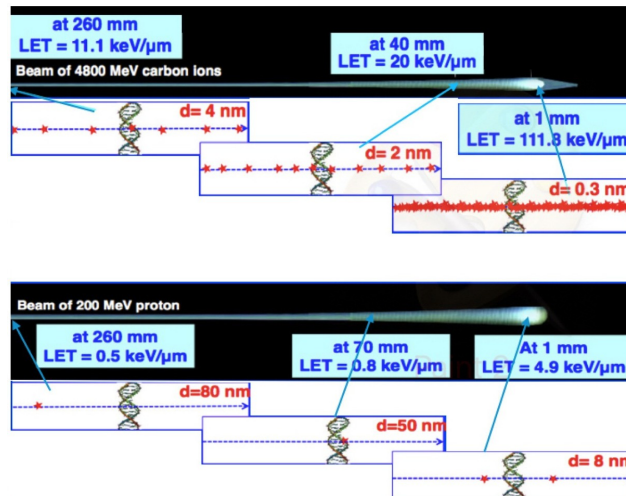


**Figure 1.9.** Comparison of the LET of beams composed of carbon ion (top) and protons (bottom);  $d$  indicates the average distance between two ionizations (adapted from [12]).

The average distance between two ionization events is of the order of hundreds of nm for low-LET radiations, for this reason they are called *sparsely ionizing particles*, while it is of the order of nm for high-LET radiations, which are called *densely ionizing particles*.

Therefore, high-LET radiations, having a higher ionization density, are more likely to break the DNA double helix. It can therefore be stated that, having the DNA helix a thickness of about 2 nm and the cell repair capacity being lower for more complex DNA damage, high-LET radiations are more likely to produce double break damage than low-LET radiations.

### 1.2.2 Cell survival curves and RBE definition

The biological effects of radiation depend on several factors, most of which are summarized in the *Relative Biological Effectiveness* (RBE). The RBE is defined as the ratio between a reference dose delivered by photons and the dose of the radiation of interest that provokes the same biological effect (Equation 1.11).

$$RBE = \frac{D_{ref}}{D_{ion}} \quad (1.11)$$

A common way to estimate the RBE of a radiation is to study cell survival curves. This is the link between dose (physical concept) and probability of survival (clinical concept). These experiments have a high significance for radiotherapy as they provide information about the radiation ability to kill cancer cells. In a standard experiment, cell proliferation is analyzed about 1–2 weeks after irradiation and cells are counted as survivors, if they have formed a colony with more than 50 daughter cells [8].

Defined  $S$ , cell survival factor, as the ratio between the fraction of surviving cells and the initial cell number, a commonly used model to parameterize the survival curves (Figure 1.10) is by using the linear-quadratic model in Equation 1.12.

$$S(D) = e^{-\alpha D - \beta D^2} \quad (1.12)$$

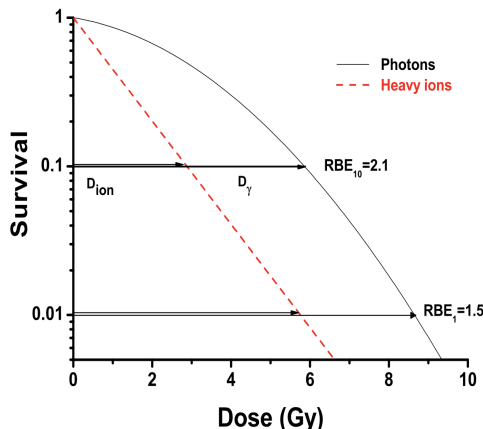
where  $D$  is the absorbed dose and  $\alpha$  and  $\beta$  are experimentally determined parameters.

 Figure 1.10 shows the determination of RBE through the analysis of the cell survival curves.

Moreover the RBE depends on different radiotherapy parameters.

First of all, Figure 1.10 shows the dependence of RBE on the dose level for heavy ions: this is higher for lower dose levels and lower for higher dose levels. This ensures that as the dose increases, the differences with the radiation taken as a reference decrease. It can be noted that the RBE also depends on the LET of the incident particles, this dependence is highlighted in Figure 1.11.

The RBE increases as the LET increases up to a maximum value, which depends on the particle we are considering, and then decreases for larger values of the LET. As the LET increases, the ionization events increase, so the ratio of surviving cells decreases and the biological effectiveness improves. Continuing to increase the LET, however, leads to a situation in which the dose released increases but the ionizing events are too close together. Therefore the ratio of cells without any particle hit, being survivors, increases resulting in a lower RBE.



**Figure 1.10.** Survival curves: fraction of surviving cells as a function of dose for photons (solid line) and heavy ions (dashed line). RBE values for cell inactivation for 10% and 1% survival level are shown [8].

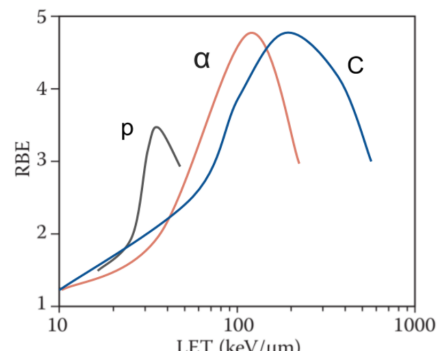


**Figure 1.11.** Experimental RBE as a function of LET for protons,  $\alpha$  particle and carbon ions [11].

In conclusion, again from Figure 1.11 we observe the dependence of the RBE on the type of particle in question: the greater the charge of the particle, the greater the value of the LET for which there will be a maximum in the RBE. With the same LET, the biological damage of  $^{12}C$  is less than that of protons.

In clinical practice a constant  $RBE=1.1$  is often used in proton treatments, considering protons biological effects not much different from photons. However, recent studies indicate that RBE variation in proton treatments should be reconsidered, since it seems relevant in particular for normal tissues in the entrance region and for organs at risk close behind the tumour [13]. Nuclear interactions might influence the proton RBE due to secondary heavier particles produced by target

fragmentation that can significantly contribute to the total dose and this leads to an undetermined increase of normal tissues complications probability. The FOOT (Fragmentation Of Target) experiment is designed to study these processes looking at target fragmentation ( $^{16}O$   $^{12}C$ ) induced by protons beam.

Carbon ions instead have an RBE up to 4-5 and are therefore used to treat more radio-resistant tumors.

### 1.2.3 Oxygenation state dependence: OER

The effects of the radiation also depend on the oxygenation state of the treated area. Growing tumors are connected by a greater number of blood vessels which ensure a sufficient supply of oxygen for their biological functions. However, tumor cells are often hypoxic, and this makes them much more resistant to radiative therapies, as the hydroxyl radical ( $OH^-$ ) which induces breaks in the DNA strand, can not form.

The oxygen effect is quantified by the OER (*Oxygen Enhancement Ratio*), defined in Equation 1.13.

$$OER = \frac{D_{hypoxic}}{D_{aerobic}} \quad (1.13)$$

where  $D_{hypoxic}$  indicates the dose required to destroy a fixed amount of hypoxic cells, instead  $D_{aerobic}$  indicates the dose necessary to destroy the same amount of cells, with a normal oxygenation. Typically the OER is equal to 3 for traditional radiotherapy and is considerably reduced for ion radiotherapy [9]

Figure 1.12 shows the studies of the cell survival curves with hypoxic and oxygenated cells carried out at the LBL in 1970 as preparation for the first treatments with heavy ions.

The difference between hypoxic and normally oxygenated cells is reduced for high LET particles and the two cell survival curves converge. The OER is a decreasing function of the particle energy and it is close to 1 for high LET particles. These behaviors were confirmed for a wide range of target ions and cells in numerous experiments carried out over the last decades. These experiments also showed that the OER is lower for heavier ions like carbon and neon than for lighter ones like helium. These considerations show that hadron beams are more suitable for the treatment of hypoxic tumor cells as they exhibit a behavior that is less dependent on excess or lack of oxygen than photons. This may be related to the increased probability that direct action for high-LET radiation occurs.

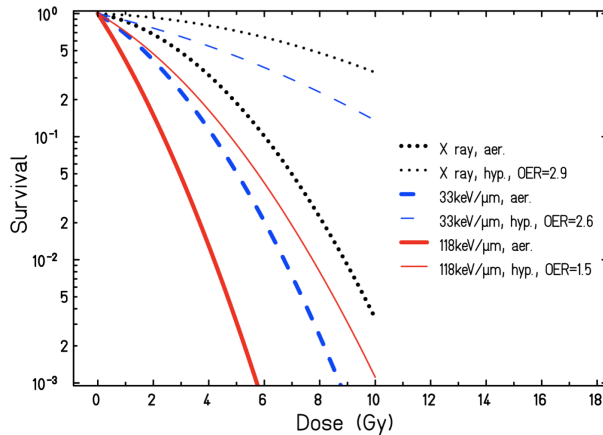


**Figure 1.12.** Influence of oxygen level on cell survival of human kidney cells under the irradiation of carbon ions at different LET values:  $33\text{keV}/\mu\text{m}$  (blue) and  $118\text{ keV}/\mu\text{m}$  (red), compared with X-rays (black) [9].

### 1.3 Treatment administration

Compared to conventional radiotherapy, PT needs more complex technologies. The beam acceleration is performed with a Linear Accelerator (LINAC), followed by a cyclotron or synchrotron:

- **Cyclotrons:** the charged particles are accelerated by an alternating electric field while following an outward spiral path in a static magnetic field. The beam is delivered with fixed energy, in short nano-bunches of  $10^2$  protons at about 100 MHz frequency. Energy variations are made by means of passive degraders and energy spread selection is made inside a spectrometer located at the exit of the cyclotron [28].
- **Synchrotron:** Synchrotrons are, until now, the only accelerators used for therapy with ions heavier than protons. They are also used for proton therapy. A synchrotron is a circular particle accelerator, in which the magnetic field, necessary to curve the trajectory of the particles, and the variable electric field, necessary to accelerate the particles, are synchronized with the beam. The variation of electric and magnetic fields allows the production of charged particle beams with different extraction energies (active beam scanning). The ion beam has a bunched structure of a few particles with a period of 100-200ns. Instead the proton beam is composed by bunches of  $10^2$  particles with a period 3-5 times smaller [28].

In Figure 1.13 a schematic view of cyclotron and synchrotron is presented.

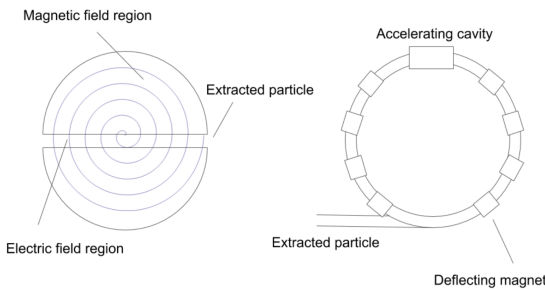


**Figure 1.13.** Cyclotron (left) and synchrotron (right) scheme.

Radiotherapy treatment planning can be described as the procedure that, using radiation beam and patient's anatomy models as input data, produces as output the machine instructions to deliver the treatment and the prescribed dose distribution in the patient.

The PT treatment is planned on the basis of a Computed Tomography scan (CT scan) of the anatomical region to be treated. CT data, in addition to allow the visualization of the internal anatomy, provide a 3D map of patient's electron density, which is needed in order to calculate the beam attenuation, and thus the dose distribution within the patient [14].

Therefore the CT scan returns a 3D map of integer values, called "Hounsfield Unit", which reflect the X-ray attenuation coefficient. After the image acquisition, the radiotherapist defines the tumour and the volume to be irradiated, delimiting the organs at risk and other structures to be taken into account. The dose, time and beam parameters are calculated by the Treatment Planning System (TPS) using an analytic algorithm. In TPS the Hounsfield Unit values of CT scan are converted in stopping power map [15], in order to correctly estimate the required beam energy. Finally, after the treatment plan has been evaluated and reviewed, the beam parameters are transferred to a database to be applied.

However the dose actually absorbed by the patient in a treatment may be different from the planned one, due to several factors. Until now to ensure complete dose coverage of the tumor, a larger volume is irradiated providing safety margins. Safety margins are chosen by each institute and may change depending on the location of the tumour and the presence of organs at risk. A great effort has been made in the last decades to develop on-line range and dose monitoring system for PT applications that allows to track during the treatment the distribution of the dose actually released in order to reduce safety margins and to provide control feedback for the energy and the position of the beam in real time. Currently only some prototypes of dose monitoring have been developed and tested in clinical treatments. This topic will be discussed in the next chapter.

## Chapter 2

# Range Monitoring techniques

The high precision of particle therapy in spatial releasing the dose delivered to the patient makes it better compared to the conventional radiotherapy but also requires high accuracy in predicting the particle range in biological tissue as a wrong estimation of the Bragg peak position can cause an under-dosage of the tumour volume and, at the same time, an over-dosage of healthy tissue surrounding the tumour. Therefore a feedback on particle range and dose release is increasingly necessary for more efficient and safe particle therapy, especially in the treatment of tumors close to organs at risk and in pediatric patients. During PT treatments the nuclear interactions between the beam and the target nuclei produce a large amount of secondary particles (photons, neutrons, charged particles) that can escape from the patient body. The characterisation of such particles in terms of kinetic energy and emission angle spectra has been object of several research in the last decades, in order to evaluate the possibility to exploit them for developing beam range verification techniques. The development of a device for secondary radiation detection and range monitoring must have certain requirements: achieve accuracy of about few mm, not interfere with the primary beam and patient positioning, last less than the treatment, not require changes to the treatment plan and the dose delivery method chosen for the patient [16].

The PAPRICA project, object of this thesis, is part of a branch of research in range monitoring technique and proposes an innovative method for range monitoring, based on prompt-gamma imaging. In the first part of this chapter the range uncertainties that can occur during the treatment are briefly summarized. In the second part the main monitoring techniques based on secondary particles detection currently under investigation from the scientific community ~~will be~~ described.

### 2.1 Range uncertainties sources

The range in tissue is associated with considerable uncertainties caused by imaging resolution, patient setup, beam delivery and dose calculation. First there are those uncertainties that are stochastic and independent of the dose calculation:

- uncertainties in beam energy (compensator design in passive beam delivery systems and beam reproducibility)
- patient alignment and setup
- relative motion of internal structures with respect to the target volume (for example due to breathing)

The uncertainties due to dose calculation are caused by:

- anatomic variations of the patient during course of therapy
- CT resolution and scan calibration
- CT artifacts
- CT grid size
- conversion of Hounsfield Unit (HU) into relative stopping power map.

In Table 2.1 the contribution of the main factors to range uncertainty is shown. Several methods have been studied to reduce the range uncertainties. However, the required accuracy has not yet been achieved and the range uncertainty will never be reduced to zero.

Source of range uncertainty in the patient	Range Uncertainty
Compensator design	$\pm 0.2$ mm
Beam reproducibility	$\pm 0.2$ mm
Patient setup	$\pm 0.7$ mm
CT imaging and calibration	$\pm 0.5$ %
CT grid size	$\pm 0.3$ %
CT conversion to tissue	$\pm 0.5$ %

**Table 2.1.** Range uncertainties [17].

## 2.2 Annihilation ~~Gamma~~ detection

A range monitoring technique is based on the use of the  $\beta^+$  emitters nuclei. As a result of fragmentation processes, the passage of the beam in the patient can create  $\beta^+$  emitters nuclei which decay emitting  $e^+$  and  $\nu_e$  as described in equation 2.1:



The positron travels for few mm inside the patient, until it annihilates with an atomic electron, producing a couple of back-to-back photons with energy of 511 keV which can be detected to reconstruct the annihilation position. The fragmentation reaction can occur both on the incident particles (projectile fragmentation) and target nuclei (target fragmentation), except in case of proton beams where only the target fragmentation is possible.

The spatial distribution along the beam line of the  $\beta^+$  emitters activity can be correlated with the Bragg curve. The different mechanism of production between protons and carbon ions affects the shape of the ion-induced activity and its correlation to the deposited dose, as shown in Figure 2.1. Radioactive nuclei, produced by the fragmentation of the target, have very low kinetic energies, and stop in proximity of the interaction point. Consequently the spatial distribution of beta decays depends only on local nuclear interactions and shows a quite flat behaviour and a falling edge in correspondence of the Bragg peak (Figure 2.1 left), due to the energy threshold of reactions. On the other hand, nuclei generated by the projectile fragmentation travel in the same direction of the beam and accumulate at their range end, resulting in a peaked spatial distribution of the beta activity (Figure 2.1 right).

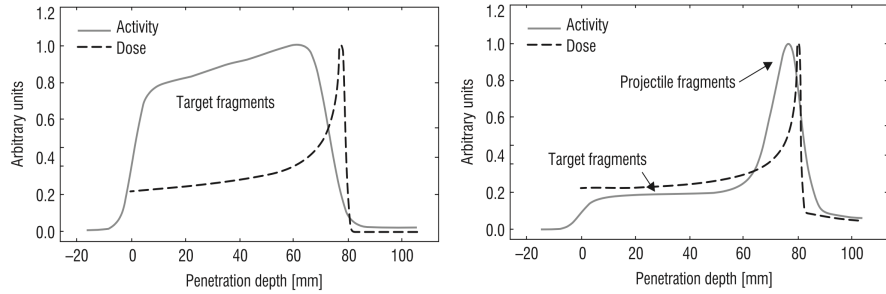


**Figure 2.1.** PMMA target activation, irradiated with a 110 MeV proton beam (left) and with a 212 MeV/u carbon ion beam (right). The solid line shows the distribution of the  $\beta^+$  activity as a function of the depth, while the dotted line indicates the dose released distribution of the primary beam as a function of the depth [18].

As mentioned, in proton therapy only the first contribution is present while in carbon ion therapy both contributions are visible but the second is dominant [19]. In both cases, the most abundant positron emitters are  $^{11}C$ ,  $^{15}O$  and  $^{10}C$  with half-lives of 20 min, 2 min and 19 s respectively.

This imaging technique for range monitoring in particle therapy can be applied in three different modes: *in-beam*, *in-room* and *off-line*. The main features and limitations of these techniques are briefly summarised hereafter. As the long decay time of the  $\beta^+$  emitting isotopes it is preferable to consider a posteriori beam range verification rather than an online range monitoring technique.

In the *in-beam monitoring* mode the detection of the annihilation gamma is performed on-line during treatment. However this mode has some intrinsic limits: low signal to background ratio and the main  $\beta^+$  emitting isotopes have a decay time that ranges from  $\approx 2\text{min}$ , for the  $^{15}O$  radioactive isotope, up to  $\approx 20\text{min}$  for the  $^{11}C$ , which are comparable with the treatment duration ( $\approx 10\text{ min}$ ). Moreover, it is not possible to install a standard full-ring PET scanner to monitor the patient during the irradiation, then only a double-head system is allowed, limiting the angular acceptance and then reducing the event collection. A low level of signal is generated, and a large background of neutrons and gamma rays emitted by the irradiated tissues is expected, which generate false coincidences and increase the dead time of the detectors [19]. Promising results with proton beams are achieved by a PET-system proposed by INSIDE (INnovative Solution for In-beam Dosimetry) collaboration, composed by two Lutetium Fine Silicate planar heads, read-out by Silicon PhotoMultipliers [20]. This device is integrated and tested in the CNAO (Centro Nazionale di Adroterapia Oncologica) treatment room.

In the *off-line* approach the  $\beta^+$  emitters activity is measured after the treatments in a nearby dedicated room [21, 22], this technique is advantageous because of the relatively low costs. Commercial full-ring PET scanners are commonly used to monitor the patient, allowing to maximise the detection angle to enhance the signal level, with fewer technological challenge compared to the development and installation of in-beam devices. However long acquisition times are needed to achieve good results, because a large fraction of the emitters decays during the time needed to move the patient from the treatment room to the PET room. Moreover, during this time, the correlation between the  $\beta^+$  activity and the released dose is reducing, resulting in a worse resolution, due to the biological wash-out. This limitation could

be reduced with the *in-room* approach, in which the PET-scanner is localised within the treatment room [23], in order to minimise the patient relocation.

## 2.3 Monitoring exploiting charged particles detection

As described in subsection 1.1.4, the target or projectile nuclei fragmentation results in the production of charged fragments of smaller charge. The target fragments are typically produced with small velocities, so that they stop with range of the micrometer order. On the other hand, the projectile fragments velocity is close to the projectile initial velocity, resulting in longer ranges. Moreover, the largest fraction of the fragments is forward peaked, and are mostly contained within a cone of few degrees with respect to the beam axis.

Therefore the fragmentation of the ion beam in the case of  $Z>1$  projectiles produces secondary charged particles, which can pass through the patient and be detected by an external device in order to monitor the beam range.

In 2014 the characterisation of the charged fragments exiting from a PMMA (Polymethyl methacrylate) target irradiated with a 220 MeV/u  $^{12}C$  ion beam has been performed at GSI facility [25]. The energy spectra and the emission profiles of the charged secondary fragments have been measured exploring two different angles  $60^\circ$  and  $90^\circ$ . For both the explored detection angles the largest fraction of the fragments results to be protons and hydrogen isotopes with emission energy that can reach values of 80-150 MeV, depending on the primary hadron beam energy. Moreover, the profile of charged particles longitudinal emission distribution is shown to be related to the beam range itself, and so to the beam energy, i.e. to the Bragg peak position (shown in Figure 2.2).

Compared to gamma radiation, charged particles have very different advantages and limitations if exploited for range monitoring techniques. The charged particles can be detected with high efficiency tracking systems. On the other hand, the statistic is lower, due to absorption into the tissues depending on their production energy, and the reconstruction spatial resolution is affected by multiple scattering within the patient. On the basis of simple geometrical considerations, the detection of charged particle at large angles with respect to the beam incoming direction corresponds to a better spatial resolution in range monitoring, however this results in a lower yield of particles as most projectile fragments are produced in the direction of the primary beam. Therefore the choice of the angle between the primary beam and the detector is always a balance between efficiency and resolution [26, 27].

The INSIDE collaboration proposed an innovative imaging concept that combines an in-beam PET scanner with a tracking system for charged particle imaging. The particle tracking is performed by the Dose Profiler. It is a multi-layer scintillating fiber tracker of charged secondary particles at CNAO facility, specifically designed and planned for clinical applications inside a PT treatment room [49].

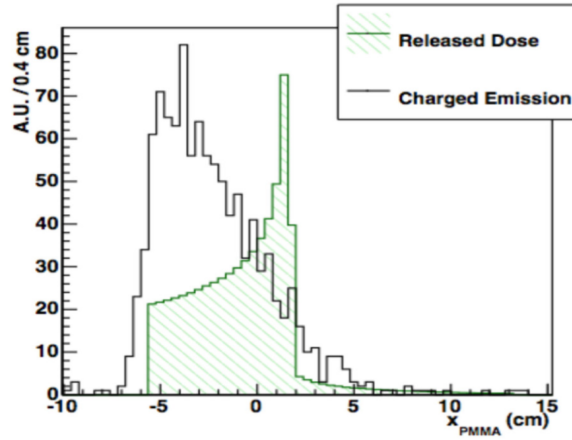


**Figure 2.2.** Longitudinal profile (solid line) of secondary charged particles as a function of the penetration in a PMMA phantom at 90° detection angle. Superimposed (hatched), it is shown the beam depth-dose distribution as from MC simulations [25].

## 2.4 Prompt Gamma

Nuclear interactions with the hadron beam can leave target nuclei in excited states. In the de-excitation processes, in addition to protons, neutrons or  $\alpha$  particles, photons in a 1-10 MeV energy range are also emitted. These photons are typically called prompt-gamma (PG), as the emission occurs in a very short time from the beam interaction, ( $\ll 1\text{ns}$ ). Several experimental and simulation studies have been carried out to measure the production yield, energy spectrum and spatial distribution of prompt-gamma, depending on particles and beam energies.

Figure 2.3 shows the energy spectrum of prompt gamma emitted by the interaction of 160 MeV proton beam impinging on water, polyethylene (PE) and polymethylmethacrylate (PMMA) targets. A large part of the energy spectrum is constituted by discrete lines. In particular the 4.44 MeV and 6.13 MeV lines are due respectively to  $^{12}\text{C}$  and  $^{16}\text{O}$  de-excitation, while the line at 2.2 MeV (particularly pronounced for PE) results from the de-excitation of deuterium after neutron capture by hydrogen and is not correlated to the primary beam range [28].

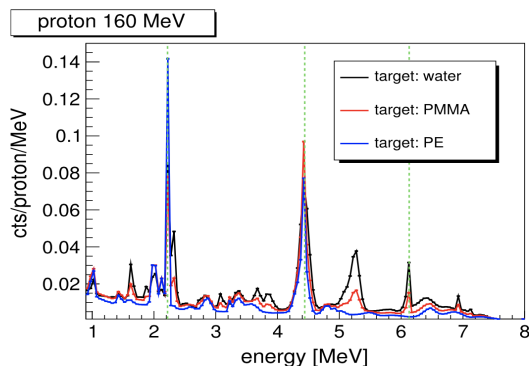


**Figure 2.3.** Energy spectra of PG emerging from water, polyethylene and PMMA cylinders (15 cm diameter, 25 cm length) irradiated by a 160 MeV proton beam. The vertical lines mark three transitions that are discussed in the text. [28].

The correlation between the prompt-gamma emission profile and the delivered dose, i.e. the Bragg peak, is shown in Figure 2.4 for different components of the spectrum.

In Figure 2.4 different prompt gamma-ray emissions along the path of proton pencil-beams in water for proton range of  $9.0 \text{ g} \cdot \text{cm}^{-2}$  are shown. In particular it illustrates the total prompt gamma-ray emission integrated over the 3.0–7.0 MeV energy window, the discrete gamma-ray profiles from  $^{16}\text{O}(p, p')^{16}\text{O}^*(6.13 \text{ MeV})$  and  $^{16}\text{O}(p, p'\alpha)^{12}\text{C}^*$  (4.44 MeV), and the dose deposited by the protons is also shown, which is described as integral depth dose in units of  $\text{Gy} \cdot \text{cm}^2$ .

The gamma emission profile has a slightly increasing distribution as a function of the depth, with a steep cut-off when reaching the Bragg peak where the primary beam particles do not have enough energy to exceed the energy threshold of nuclear reactions. Photons at 4.4 MeV have the greatest spatial correlation with deposited dose and therefore are the most suitable component for monitoring the primary beam range.

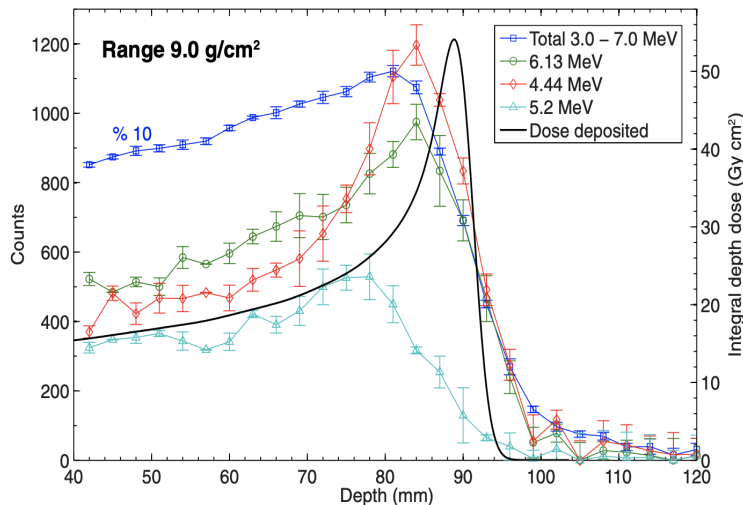


**Figure 2.4.** Spatial distribution of prompt-gamma emission for the different components of the spectrum, obtained with a proton pencil-beam with 9 cm range impinging on water [30].

Thanks to their prompt emission, gamma rays represent a natural choice for online, in-beam monitoring, as the metabolic wash-out does not affect the correlation between emission profile and dose. Moreover, due to their energy they penetrate the patient with a quite low scattering probability, preserving their direction at production.

Furthermore two main factors can limit the technique performances. First, a large uncorrelated background due to secondary neutrons, which can be discriminated from prompt-gamma only with time-of-flight techniques, reducing the signal-to-noise ratio. Second, the inherent difficulty in tracking, so the inability to detect the gamma ray without the photon being absorbed (photoelectric effect) or changing direction (Compton scattering). This feature requires the use of collimators to determine the photon direction (imaging systems) or the measurement of different properties of the emitted prompt-gamma (non-imaging systems). A quick review of the techniques using prompt-gamma detection to improve hadrontherapy follows hereafter.

### 2.4.1 Imaging system

Prompt-gamma imaging devices can be divided into systems based on measuring the PG direction through mechanical or electronic (Compton cameras) collimation, respectively. These techniques are briefly described below.

#### Mechanical collimation

Several different collimators geometries have been investigated, in order to design an efficient collimator for a wide energy spectrum and to collect a sufficient number of events. Different mechanical collimation imaging systems have been studied and tested: using a pinhole, linear slit or multiple slits [28].

The principle of the pinhole camera, known from classical optics, can also be adapted for prompt gamma imaging. A first experiment has been performed at a 50 MeV proton beam impinging on a water target [32]. The prompt gamma rays were detected with a scintillation detector behind a pinhole aperture, located to view the endpoint of the proton range. The pinhole configuration allows in principle 2D images of the prompt gamma distributions. For the purpose of range monitoring, however, the 1D projection along the beam axis is sufficient. This changes the pinhole aperture to a single slit of the knife-edge type. An example of a six-knife edge slit camera has been recently developed by a collaboration between the Politecnico di Milano and Ion Beam Applications (IBA) and tested on patients. The device consists of a Tungsten collimator and a Lutetium-Yttrium Oxyorthosilicate (LYSO) slice detector (Figure 2.5). The main limitation is the dependence of the resolution on the alignment of the chamber with respect to the beam range. [34].

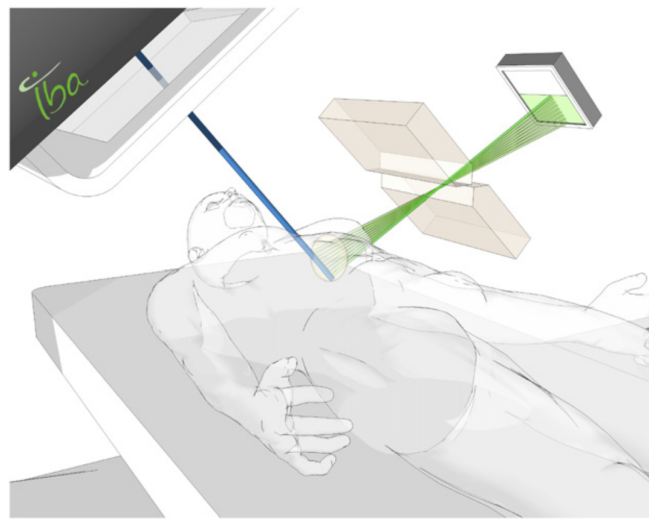


**Figure 2.5.** Linear slit chamber developed by the collaboration between the Politecnico di Milano and IBA [34]. The blue line represents the proton beam, the green line represents the prompt gamma rays that pass through the slit collimator placed perpendicular to beam direction.

The linear slit camera is not capable to acquire the full field of view during a single measurement, but the system has to be moved in different positions. To overcome this limitation was proposed a multi-slit collimation device [33], that can be made large enough to cover the full field of view.

The linear slit camera has higher counting efficiency compared to the multi slit one, being able to estimate the beam range even for  $10^7$  protons for a single proton pencil beam. On the other hand, the multi slit camera shows lower efficiency compared to the linear one, as it can estimate the beam range correctly only when the number of the protons is at least  $10^8$ . However, for enough number of protons, an accuracy of the order of 1 mm on a single proton pencil beam has been achieved with a multi slit camera [35].

### Compton cameras

Active or electronic collimation is an imaging techniques that exploits the Compton scattering of a prompt-gamma to determine its direction. The Compton effect is the elastic collision between a photon and an electron of the medium.

When a photon of energy  $E_\gamma$  scatters, it produces a recoil electron with kinetic energy  $E_e$ , lowering the incoming photon energy down to  $E_{\gamma'} = E_\gamma - E_e$ . The incident photon is deflected by an angle  $\theta$  according to the relation 2.2:

$$\cos(\theta) = 1 - m_e c^2 \left( \frac{1}{E_{\gamma'}} - \frac{1}{E_\gamma} \right) \quad (2.2)$$

Where  $\theta$  stands for the scattering angle between the  $e^-$  and the  $\gamma$ . Typically, a Compton camera consists of one scatterer detector and one absorber detector, as schematically shown in Figure 2.6.

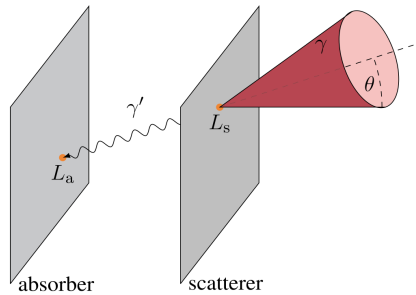


**Figure 2.6.** Concept of a typical Compton-camera [36].

The incoming photon  $\gamma$  interacts in the scatterer layer, generating a photon  $\gamma'$  with lower energy which is absorbed in the other layer. The two interaction points provide the  $\gamma'$  direction. The measure of  $E_{\gamma'}$  allows to narrow the direction of emission of the primary gamma ray on the surface of a cone with opening angle  $\theta$ , axis defined by the direction of the scattered gamma and vertex at the point of scattering Compton. Compton cameras suit well with the prompt-gamma energy range, where Compton scattering is typically the most probable kind of interaction in low Z material and can also provide 3D information on the photon emission point. However, the instrumentation requirements in terms of spatial, time, and energy resolution for the detectors of a Compton camera are high, and the reconstruction algorithm is complex as the reconstructed vertex of the photon generation is obtained via the superposition of multiple cones.

An example of Compton Camera is described in [37]. The detector, shown in Figure 2.7, is based on a cerium-doped Lanthanum Bromide  $LaBr_3(Ce)$  scintillation crystal acting as absorber ( $50 \times 50 \times 30 \text{ mm}^3$ ), preceded by a stack of 6 double-sided silicon strip detectors as scatterers. The scintillation material is chosen for its good

energy resolution and it is read out by a multi-anode photomultiplier. Instead, the scatter detectors ( $50 \times 50 \text{ mm}^2$  active surface) are 128 fold segmented on each side.

A reconstruction efficiency of  $10^{-3} - 10^{-5}$  can be expected for a stack of 6 double-sided silicon strip detectors as scatterers in the energy range of  $E_\gamma = 1\text{-}6 \text{ MeV}$ . In a typical scenario for laser-accelerated proton pulses with  $E_p = 100 \text{ MeV}$  hitting a water phantom, about 0.04 prompt gamma rays per primary proton will be emitted from nuclear reactions and, in this case, shifts in the proton range as small as 3 mm were detectable [37].

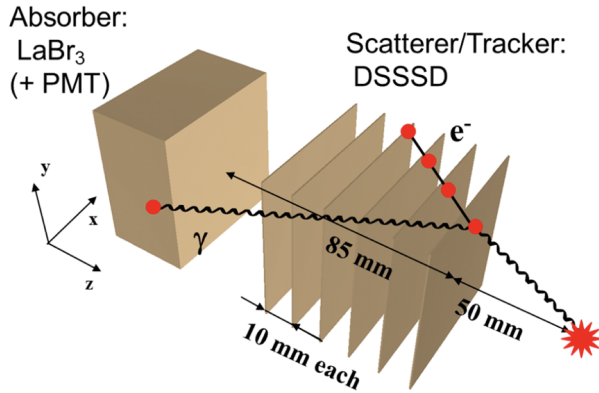


**Figure 2.7.** Schematic view of the Compton camera layout, consisting of a stack of 6 double-sided silicon strip detectors as scatterer and a  $\text{LaBr}_3$  scintillation crystal acting as absorber [37].

#### 2.4.2 Non-imaging systems

As mentioned before, a non-imaging system is based on the different properties of gamma radiation. In this section three different methods of non-imaging systems are described.

##### PGT (*Prompt-Gamma Timing*)

PGT is an alternative approach for range verification, based on the determination of the beam particles transit time within tissue. Beam particles entering material cause the emission of prompt-gamma along their path, until they are stopped. At beam energies used in PT, the time difference  $\Delta t$  between the entrance of the proton into the target and the arrival of the prompt-gamma to the detector is measurable, being on the order of 1-2 ns for protons with a range of 5-20 cm.  $\Delta t$  is the sum of the proton transit time  $t_p(z)$ , defined as the time of the proton between the entry and the interaction with a nucleus, the decay time of the nucleus emitting gamma and the time needed by the photon to reach the detector (Figure 2.8). The distribution of  $\Delta t$  will therefore depend on the spatial distribution of the gamma, which is correlated to the Bragg peak.

In a facility with a pulsed beam the time of flight is measured with an uncollimated scintillation detector and allows to deduce the emission point of the prompt-gamma. The simulations demonstrated the feasibility of the principle, showing a correlation between the beam energy, i.e. the range, and the measured time of flight [38].

The first tests of PGT in clinical environment have given promising results, in particular experiments were carried out in the treatment room of the University

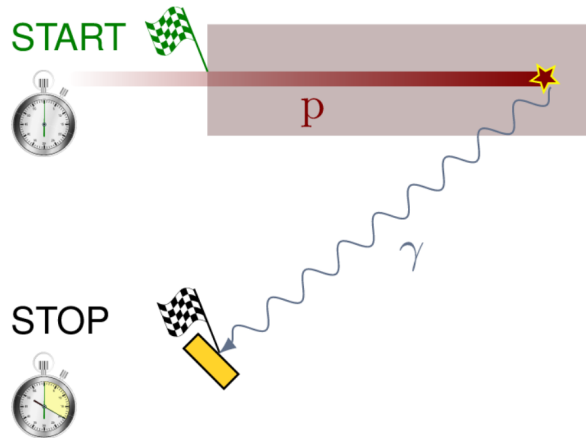


**Figure 2.8.** Concept of the Prompt Gamma Ray Imaging [36]. The time difference between the proton entrance in the target and the prompt-gamma detection is correlated to the emission point.

Proton Therapy Dresden in order to test the precision of the PGT method, as well as the capability of detecting range shifts due to heterogeneities in the target. A pencil beam scanning plan was delivered to a target without and with cylindrical air cavities of down to 5 mm thickness [38] and the range shifts of the proton beam induced due to the material variation could be identified from the corresponding time profiles. Finally the main advantage of this technique is the possibility to discriminate neutrons, however the achievable precision of this technique is limited both by detector resolutions and the need for a pulsed beam, implying the knowledge of the accelerator.

### PGPI (*Prompt-Gamma Peak Integral*)

In PGPI the peak integrals of prompt gamma-ray TOF distributions are exploited to estimate the proton range, in order to detect deviations from the prescribed treatment during particle therapy and to avoid overdosage.

In this method the TOF spectra of the prompt gamma is considered. The peak in the measured spectra is due to prompt gamma-ray production in the target and it is then integrated fixing an interval.

Test measurements have been performed at a clinical cyclotron with 65 MeV protons impinging on a PMMA (Poly-methyl-methacrylate) target with variable thickness (the experiment is fully described in [40]), and have demonstrated the variation of the peak integral with the variation of the proton range inside a PMMA target.

From the experiment two spectra correspond to different positions of the beam respect to the target can be observed , when at 0 degree the beam is hitting the part of the target with the maximum thickness, and when at 90 degree it is traversing no material (Figure 2.9)

A change in the proton energy will be reflected in the prompt gamma TOF spectra, in fact in Figure 2.9 the mean TOF value of the peak is shifted by 2-3 ns between 90 and 0 degree.

Further simulation studies show that a combination of the signals from multiple detectors may be used to detect a misplacement of the target. In fact, the number of events observed by each detector depends on the distance from the emission points

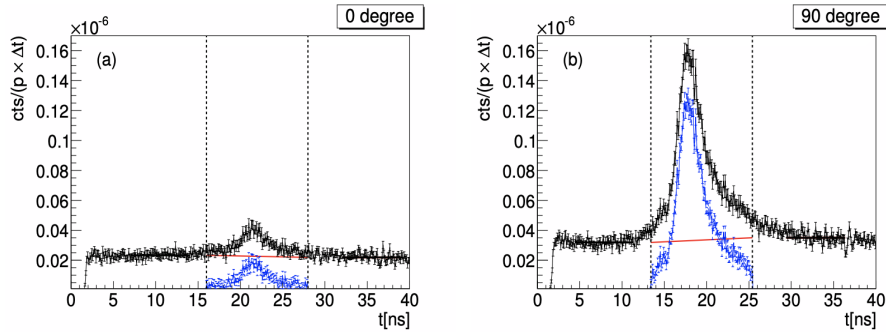


**Figure 2.9.** TOF spectra (in black) corresponding to different positions correspond to the maximum thickness (a) and the hole (b). The ordinate displays the counts per incident proton and time bin  $\Delta t = 0.1$  ns. After subtracting the background (in red), the signals (in blue) corresponding to prompt gamma-ray emission from the target are integrated within the limits given by the vertical dashed lines [40].

of the gamma prompts and an analysis of the difference in count rate allows to deduce information about the emission profile

Until now this technique has been demonstrated in a simplified test case and its applicability in clinical scenarios has not yet been evaluated.

### PGS (*Prompt-Gamma Spectroscopy*)

PGS is a method based on the identification of characteristic prompt gamma spectral lines and their relative contributions. In PGS the ratio between the spectral lines is exploited in order to estimate the ratio between the cross sections of the different reaction channels, thus deduces the beam energy and the crossed tissue composition.

Using experimentally determined nuclear reaction cross sections and a Monte Carlo simulation, a detailed model of the expected gamma-ray emissions is created for each individual pencil-beam. The absolute range of the proton pencil-beams is determined by minimizing the discrepancy between the measurement and this model.

In measuring devices an appropriate collimator system allows to analyse separately different slices of the beam (as in [39]). In [39] a prompt gamma-ray spectroscopy system was developed in order to achieve millimeter accuracy in proton range verification under clinically realistic conditions. Here gamma-rays are detected using eight detector modules, each consisting of a  $LaBr_3(Ce)$  (cerium-doped Lanthanum Bromide) scintillation crystal. Differential cross sections were measured for prompt gamma-ray lines from proton-nuclear interactions. These cross sections were used to model discrete prompt gamma-ray emissions along proton pencil-beams. By fitting detected prompt gamma-ray counts to these models, it was determined the beam range and target composition.

However this method still has to face the issues of available statistics for PG line, and the presence of mixed-beams with heterogeneities.

## Chapter 3

# The PAPRICA project

~~As mentioned before different techniques have been developed in order to exploit the prompt-gamma rays. However all the before mentioned approaches suffer from the large neutron background and low signal-to-noise ratio that avoid to reach a sufficient accuracy in monitoring the beam range, for this reason the PG have not yet entered in the clinical routine. Due to the energy spectrum of prompt gamma rays it is reasonable to consider the utilization of pair production events to reconstruct the origin of these prompt gamma. This approach was explored for PG imaging once in [43] with a simplified setup.~~

The aim of the PAPRICA (*PAir PRoduction Imaging ChAmber*) project is to investigate the feasibility of an online beam range monitoring in proton therapy, which exploits the Pair Production (PP) mechanism to detect and backtrack prompt-gamma radiation. This technique has been developed in astrophysics applications for high energy cosmic photon imaging (from 10 MeV to a few GeV) [41, 42], but has never been explored in the PG energy range. The PAPRICA detector has very different objectives and constraints compared to cosmic-rays detectors and, in particular, it needs to be a device that could operate in a clinical environment.

PAPRICA exploits the PG with energy greater than 4 MeV, for which the PP cross-section becomes significant. As shown in section 2.4, such gammas are the ones more correlated with the Bragg peak: this allows to reduce the background from the lower-energy photons induced by neutrons-nucleus reactions, which are unrelated to the Bragg peak. The topological signature of the pair allows also for neutrons rejection without time of flight information, opening the possibility of exploiting such range monitoring technique both in proton and in carbon ion therapy. In addition, no collimations technique, nor mechanical nor electronic are needed to back-track the incoming photons to their production point. The PAPRICA detector, whose design has been optimised by means of MC simulations, is currently under construction, delayed due to the COVID-19 pandemic. In this chapter the principle of operation of PAPRICA is described, reminding the physics ~~process~~ of the pair production. Then, the PAPRICA device is presented, describing the sub-detectors of which is composed.

### 3.1 Pair Production in PAPRICA

~~As mentioned, the pair production effect is at the basis of the PAPRICA project and it is described in this section.~~

When  $E > 2m_e c^2$  the threshold for the production of electron-positron pairs

opens ( $e^+e^-$ ). The creation of pairs can not take place in vacuum: due to the difference between the initial invariant mass (which must be zero) and the final state that contains the two electrons, the production must therefore take place in the presence of a nucleus that absorbs the momentum in excess. The mechanism is explained in a better way hereafter.

A scheme of a pair production event is shown in Figure 3.1.

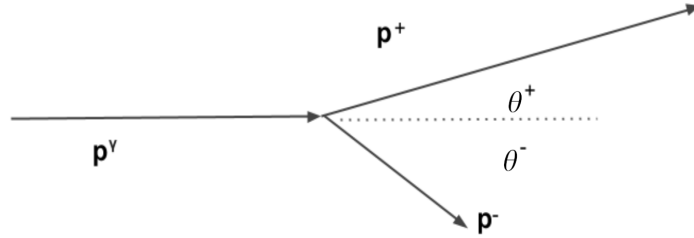


**Figure 3.1.** Pair production:  $p^\gamma$ ,  $p^+$  and  $p^-$  are respectively the gamma, positron and electron momentum while  $\theta^+$  and  $\theta^-$  are the polar angles between the gamma direction and the leptons directions.

In pair-production mechanism the energy and momentum conservation laws imply:

$$p^\gamma = p^+ \cos\theta^+ + p^- \cos\theta^- \quad (3.1)$$

$$p^+ \sin\theta^+ = p^- \sin\theta^- \quad (3.2)$$

$$p^\gamma = \sqrt{(p^+)^2 + m_e^2} + \sqrt{(p^-)^2 + m_e^2} \quad (3.3)$$

Equation 3.3 sets a cut-off equal to  $2m_e = 1.022$  MeV (with  $m_e$  electron mass) in the photon energy for the generation of an electron-positron pair. As mentioned, the conservation of energy and momentum can not be achieved simultaneously without the introduction of a third body acquiring part of the energy and momentum of the photon. This body may be a nucleus. The nucleus is much more massive than the leptons involved and can absorb a fraction of the photon momentum without a significant increase in kinetic energy. The momentum of nucleus recoil is given by:

$$p^N = p^\gamma - p^+ \cos\theta^+ - p^- \cos\theta^- \quad (3.4)$$

Let consider the simple case in which the electron and the positron are emitted at the same angle with respect to the direction of the photon. The angle between the two leptons can be defined as  $\theta \equiv 2\theta^+ = 2\theta^-$ . From Equation 3.2 and Equation 3.3  $p^+ = p^- \equiv p$  and  $E^+ = E^- = E^\gamma / 2$ . Therefore, substituting the values, the nucleus recoil becomes:

$$p^N = p^\gamma - 2p \cos \frac{\theta}{2} \quad (3.5)$$

$$p^N = E^\gamma - 2 \sqrt{\left(\frac{E^\gamma}{2}\right)^2 - m_e^2 \cos^2 \frac{\theta}{2}} \quad (3.6)$$

The result obtained with this simple model shows that the nucleus recoil increases with  $\theta$  and decreases with  $E^\gamma$ . The cross-section of pair production is increasing with the energy of the photon and proportional to the square of the atomic number of the nucleus involved ( $Z^2$ ). Bethe and Heitler calculated the pair production cross section using the Dirac theory, as function of photon and particles energy. In the calculation they considered a point-like nucleus and neglected the effect of electron screening on nucleus charge. Other models have been then developed to take into account the effects of nucleus shape and electron screening [44]. Finally in Figure 3.2 the cross section dependence on the fraction of photon energy acquired by the electron ( $\epsilon = \frac{E^-}{E^\gamma}$ ), called reduced energy, is shown. The Bethe-Heitler theory predicts that the pair-production cross section, as a function of the electron reduced energy, is symmetrical around  $\epsilon = 1/2$ . This trend is reasonably right only for photon energies larger than  $\approx 5$  MeV. For lower photon energies, the effect of the electrostatic field of the atom (which slows down the electron and accelerates the positron) becomes increasingly important, with the result that electron energy distribution becomes asymmetrical with a mean value less than 1/2.

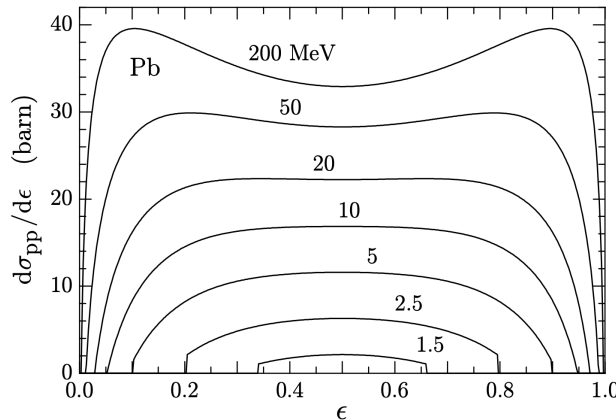


**Figure 3.2.** Cross section dependence on electron reduced energy in lead (Pb). The trends for different photon energy are shown [46]

The cross sections of gamma interactions depends on the energy of the photon and on the atomic number of the material involved (as shown in Figure 3.3). At low energy ( $\leq 0.5$  MeV) and high atomic number the dominant interaction is the photoelectric effect. The relative importance of the Compton effect increases with energy, especially for low atomic number materials. Pair production has an energy threshold of 1.022 MeV and it is the dominant effect for high energy ( $\geq 5$  MeV) and high atomic number.

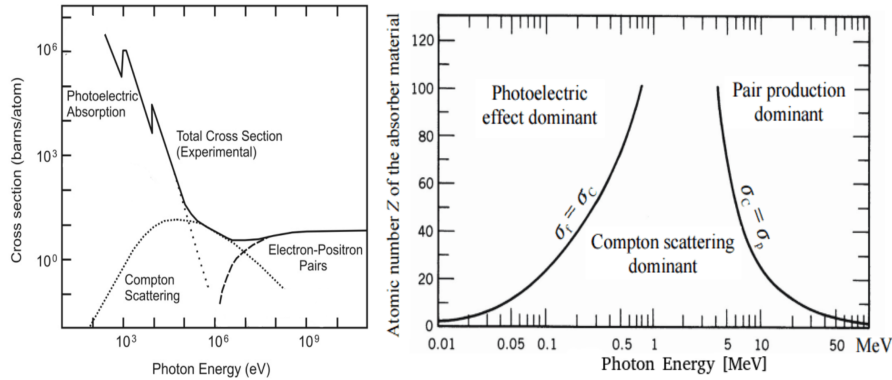


**Figure 3.3.** Cross section of the three main types of gamma-ray interaction (left). Relative importance as a function of the photon energy and atomic number of the absorber (right) [45].

## 3.2 The PAPRICA detector

The goal of PAPRICA is to detect the electron-positron pair, generated in the prompt-gamma pair production, and reconstruct the incoming photon direction measuring its four-momentum. The PAPRICA chamber is composed by three sub-detectors, as shown in Figure 3.4.

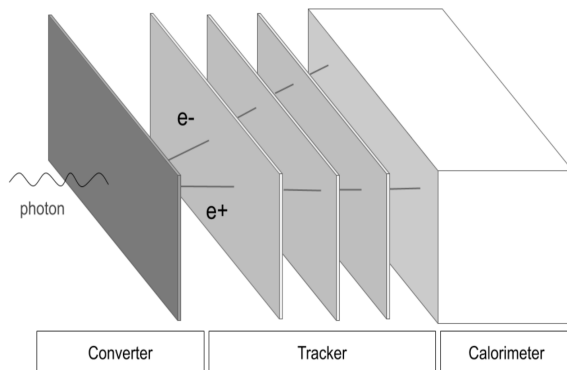


**Figure 3.4.** Sketch of the PAPRICA design: the converter, the tracker and the calorimeter blocks are shown.

First a converter layer, made of a high  $Z$  material to maximise the pair-production cross section ( $\sigma_{PP} \propto Z^2$ ), is used as a target for the photon conversion in a  $e^+ e^-$  pair. Then a tracking system, consisting in a set of three tracking stations based on silicon pixel detectors, provides the  $e^+ e^-$  direction and the interaction vertex. Finally a matrix of pixelated plastic scintillator acts as a calorimeter, measuring the residual kinetic energy of the lepton pair. The incoming PG momentum is obtained using the Equation 3.7

$$\vec{p}^\gamma = \vec{p}^+ + \vec{p}^- \quad (3.7)$$

The momentum acquired by the nucleus is a not-accessible parameter and

consequently must be neglected, introducing an intrinsic limit in PG production point reconstruction. The PG 4-momentum resolution is also affected by the multiple scattering suffered by the lepton pair as it exits from the converter layer and crosses the tracking stations. In order to optimize the PAPRICA performance, the detectors material and geometry have been set by means of a Monte Carlo (MC) simulation developed with the FLUKA software (described in section 4.1). However the detector is still under construction. A description of the three detectors composing the PAPRICA chamber is presented hereafter.

### 3.2.1 Converter

The production of an electron-positron pair takes place in the converter. After pair production, electron and positron cross the converter along the direction of the original gamma prompt and, before exiting the converter, can undergo variations in energy and momentum. The main interaction mechanisms of electrons and positrons with the medium are the multiple scattering with the electrons of the medium and the annihilation of the positron with an electron. These interactions lead to a loss of information of the momentum and the energy of the particles. Moreover, the pair production depends to the atomic number of the medium ( $\propto Z^2$ ), while multiple scattering cross section is proportional to  $Z$ . Finally for thin layer, the number of pair generated is proportional to thickness  $\delta z$  as:

$$N_{PP} = \sigma_{PP} \cdot \delta z \cdot N_{PG} \quad (3.8)$$

where  $\sigma_{PP}$  is the pair-production cross section and  $N_{PG}$  the number of prompt-gamma. At the same time multiple scattering depends on the number of collisions and so on the distance that electron and positron must travel. Therefore the converter layer has been optimised in terms of material (atomic number  $Z$  and density  $\rho$ ) and thickness in order to balance the pair production efficiency, maximising the number of PP interactions, while minimising the converter MS. The Lutetium-Yttrium Oxyorthosilicate, also known as LYSO, is an inorganic scintillating crystal with chemical formula  $Lu_{2(1-x)}Y_{2x}SiO_5$  ( $Z = 66$ ,  $\rho = 7.1 \text{ g/cm}^3$ ) and it has been chosen over tungsten W ( $Z = 74$ ,  $\rho = 19.3 \text{ g/cm}^3$ ) and lead Pb ( $Z = 82$ ,  $\rho = 11.3 \text{ g/cm}^3$ ). LYSO is an active material, i.e. able to generate a signal that can be detected when a charged particle crosses it, while W and Pb are passive one. An active converter is more advantageous than a passive one because it allows to have a trigger on pair production, i.e. to determine which events detected in the tracker can be associated with the generation of an electron and positron, by selecting the events in which a coincidence signal occurs in the converter and in the calorimeter in order to reduce the background events. The converter layer will be composed by  $\approx 130$  LYSO fibers placed side by side,  $1.5 \times 1.5 \times 50 \text{ mm}^3$  each, for a total surface of  $\approx 5 \times 20 \text{ cm}^2$  and 1.5 mm thickness. The fibers will be read by two 64-channels MultiAnode PhotoMultiplier (MAPM) (Hamamatsu H8500). Each LYSO fiber will be painted with white reflector (EJ-510) to prevent from optical cross-talk and coupled to a MAPM anode using optical fibers. The MAPMs power supply and read-out will be addressed by a system inherited by the Dose Profiler, a multi-layer scintillating fiber detector developed for range monitoring purposes in PT (fully described in [49]).

### 3.2.2 Tracker

The purpose of the tracker is to track the electron and positron, allowing to determine their momentum direction. The tracker has to have high tracking efficiency

and high spatial resolution, while it has to minimize the multiple scattering and the energy loss inside the tracker itself.

The detector chosen for particle tracking is based on ALPIDE (ALice PIxel DEtector) chip [48] developed by the ALICE (A Large Ion Collider Experiment) collaboration at CERN. Each chip is a  $15\text{mm} \times 30\text{mm}$  MAPS (Monolithic Active Pixel Sensor), implemented in a 180 nm CMOS (Complementary Metal-Oxide Semiconductor) imaging sensor process. The sensor is segmented in  $512 \times 1024$  pixels of  $29\mu\text{m} \times 27\mu\text{m}$  each. The interface, control and reading function is implemented in a periphery circuit region of  $1.2\text{mm} \times 30\text{mm}$ , which also constitutes a dead area of the sensor for crossing particles.

The ALPIDE has a tracking efficiency for Minimum Ionizing particles greater than 99%, with a fake-hits rate less than  $10^{-6}$  per pixel and event [48].

The tracker will consist of 3 planes, called HIC (Hybrid Integrated Circuit). Each HIC will be a matrix of  $7 \times 2$  ALPIDEs for a surface of  $21 \times 3 \text{ cm}^2$ . The HIC will use Cu-clad Pyralux, with a  $75\mu\text{m}$  thick substrate of Kapton polyimide film and copper foils  $18\mu\text{m}$  thick on both sides. The off-detector readout will be managed by a board that will interface with the DAQ (Data AcQuisition) PC via an ethernet link. The powering of the tracker layers will be managed by a Power Board, providing the possibility to power and monitor the voltages and currents for each layer independently.

The inter-plane distance has been optimised in order to meet the converter constraints and the minimum distance of  $\approx 2 \text{ cm}$  has been determined, it maximises the collectable pair statistics, geometrically selecting pairs from PG with energy grater than 4 MeV. Indeed angular acceptance, and consequently efficiency, decreases as the inter-plane distance increases causing a larger loss of the pairs.

### 3.2.3 Calorimeter

The purpose of the calorimeter is to measure the kinetic energy of the leptons as well as to provide a trigger for the data acquisition. The calorimeter must be pixelated in order to detect the electron and positron separately, and distinguish between the background events.

The material and size of the calorimeter have to be chosen in order to minimize the backscattering of positron and electron from the calorimeter surface. When a lepton is backscattered it releases only a fraction of its kinetic energy in the calorimeter, preventing to properly reconstruct the lepton kinetic energy. Moreover, it can go back through the HIC ALPIDE, spoiling the reconstruction process.

Therefore an organic plastic scintillator (EJ-200, Z=4,  $\rho=1.023 \text{ g/cm}^3$ ) with low atomic number has been chosen. The scintillator will be segmented in 256 rods  $6 \times 6 \times 50 \text{ mm}^3$ , arranged in a  $8 \times 32$  matrix, composing a surface of  $\approx 5 \times 20 \text{ cm}^2$ , allowing for intercepting more than 98% of the pair traversing the three HIC planes. Each rod will be painted with white reflector (EJ-510) to prevent from the optical cross-talk. The rod side has been determined from the average distance between the  $e^+ e^-$  tracks crossing the calorimeter surface, while the length is the one needed to absorb the maximum energy pair. Four MAPMs Hamamatsu H8500, whose anode size match with the rod size, will be coupled to the scintillator matrix to detect the scintillation light. The calorimeter will share the read-out chain of the converter.

### 3.2.4 Converter/Calorimeter read-out

As previously mentioned, the converter and the calorimeter share the read-out system, whose layout is inherited by the Dose Profiler [49].

The MAPMs read-out is provided by a set of ASICs (Application Specific Integrated Circuit) with 32 channels each, named *BASIC32-ADC* (BASIC). The MAPMs have 64 channels so, 12 BASIC (4 for the converter and 8 for the calorimeter), housed in separated boards which also include a HV module, are used to read out-all the system.

This BASIC boards are interfaced with control FPGAs (Field Programmable Gate Array) used for the *BASIC32-ADC* configuration and read-out. One FPGA board is necessary for 4 BASIC boards.

Finally, a board named *Concentrator* is used as a master unit to generate and to distribute the trigger signal, to collect the data of the FPGA and to manage the communication with an external PC used for the data storage and processing through an ethernet link.

The electronics is organised following the architecture shown in Figure 3.5.

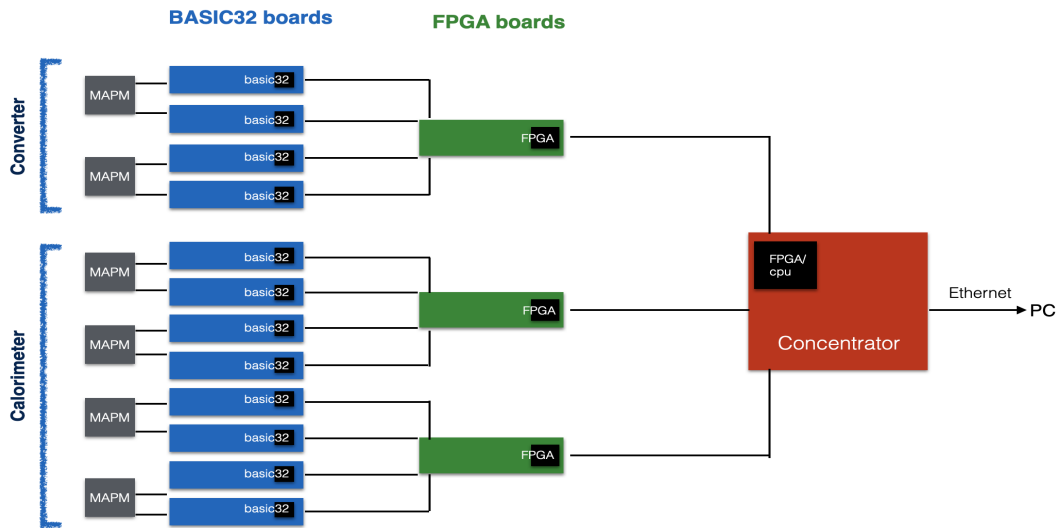


**Figure 3.5.** Schematic view of the read-out electronics.

The different part of the electronics are briefly described herafter.

- **BASIC:** The BASIC32-ADC (BASIC) is a self-triggering, 32-channel ASIC, purposely developed to read-out Photo- Multiplier detectors in medical imaging applications [50]. The ASIC provides the integrated charge, which is registered for each channel that exceeds an adjustable threshold, providing a trigger signal, which is asserted when at least one channel overcomes the set threshold.
- **FPGA:** the BASIC-boards are coupled with the FPGA boards. The FPGA assignments are basically to sent the configuration to the BASICs and to perform the data read-out. The logic of the BASIC internal trigger and of the data valid signals are output by the FPGA towards the Concentrator, respectively for the global trigger signal generation and to manage the read-out procedure operated by the Concentrator. The core of the system is formed by a set of control register and two RAM (Random Access Memory) blocks. The RAM blocks are used to store the configuration words that have to be input to the BASICs. As soon as the trigger arrives, a signal is sent to the BASIC

to enable the read-out procedure, and other signal is sent to the Concentrator, remaining active until the read-out is completed.

- **Concentrator:** The FPGA boards are connected to the Concentrator board. The core of the board is constituted by a system which provides the access to over 100 user I/O pins through three connectors on the backside of the module. It includes an Ethernet interface, USB, and 1GB RAM block.

Figure 3.6 shows a system composed by BASIC boards and FPGA board, while Figure 3.7 shows the concentrator board.

The concentrator is used to build a trigger which is generated on the base of the signals coming from the FPGAs. The trigger logic is fully configurable, and can be changed before each data acquisition according to the necessity. Two triggering strategies could be implemented: a *stand-alone triggering mode* in which the information from each ASIC is combined and used to decide if the event is of interest, and an *external triggering mode* in which the board readout is activated by an external input.



**Figure 3.6.** Picture of a system with BASIC boards (blue) and FPGA board (green).



**Figure 3.7.** Picture of the concentrator (red) board.

## Chapter 4

# Trigger and event selection

The PAPRICA chamber aims to select the events in which a prompt-gamma converts in a  $e^+ e^-$  pair in the converter layer, requiring that both the leptons are absorbed by the calorimeter to allow the incoming gamma kinematic reconstruction. Despite the PAPRICA events of interest have a strong experimental signature, i.e. a couple of reconstructed tracks in the tracker<sup>5</sup>, the tracking system can not be used for triggering. The presence of such pattern in the tracker can be used only for an off-line selection. In a PT treatment, several secondary particles escape from the patient body (neutrons, recoil protons) and may produce a signal in the converter and in the calorimeter. These particles have rates that can even reach  $10^5 - 10^6$  Hz, considering typical therapeutic rates of a proton beam are of  $10^{10}$  protons/s. The feasibility of the technique proposed by PAPRICA will be tested in the next future using phantoms irradiated by proton beams at therapeutic intensity/energy. In my thesis I evaluated the main background contributions expected in such scenario by means of a Monte Carlo Simulation performed with the FLUKA software [51]. Using the MC outcome, I estimated the PAPRICA detection efficiency and the background level considering different possible trigger strategies. In the first part of this chapter, the topology of events is presented, showing the energy released in the calorimeter and converter detectors. Then, the results in terms of efficiency and purity will be shown for different trigger strategies.

### 4.1 FLUKA code

The FLUKA code is a general purpose Monte Carlo code for calculation of particle transport and interactions with matter, covering an extended range of applications spanning from proton and electron accelerator shielding to target design, calorimetry, activation, dosimetry, detector design, Accelerator Driven Systems, cosmic rays, neutrino physics, radiotherapy [51, 52]. FLUKA is based on updated physical models, based as far as possible on well tested microscopic models. The microscopic approach preserves correlations among particles physical quantities, and it provides predictions where no experimental data are available. The physical models are fully integrated in the code and cannot be modified. However, a set of user interface routines can be used to customise the software and control each step of the simulation. Complex geometries can be managed, thanks to an improved version of the Combinatorial Geometry (CG) package. Various visualisation and debugging tools are also available, as the graphical interface Flair, which includes the high-level management of the entire simulation process, the geometry generation and material assignment.

### 4.1.1 PAPRICA simulation

The PAPRICA expected performances has been evaluated simulating the interaction of a 160 MeV proton beam impinging on a PMMA (Polymethyl-methacrylate) thick target  $5 \times 5 \times 20\text{ cm}^3$ , which well approximates the density and the atomic characteristics of biological tissues. The simulation setup is shown in Figure 4.1.

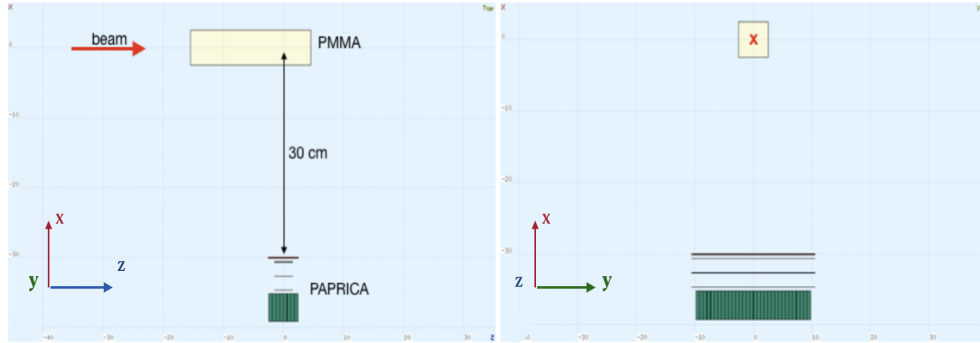


**Figure 4.1.** View of the FLUKA simulated geometry. The converter is shown as a black line, then the tree tracker planes are shown and the calorimeter is shown in green. The beam direction (in red) is along the positive z-axis. The XZ (left) and XY (right) views are shown.

The PMMA is positioned along z (beam direction) in order to have the Bragg peak at the origin of the coordinate reference system. The detector is positioned at  $90^\circ$  with respect to the beam direction, in order to not affect the reconstruction with the beam lateral spread and to select the prompt photons emitted from the distal part of their spatial emission distribution. The distance of the converter from the coordinate system origin is 30 cm, as it is known that distances of the order of 30 cm are compatible with the monitor operation inside a treatment room [53].

The energy spectrum of the prompt gamma coming out of the PMMA is shown in Figure 4.2. The energy peaks due to the de-excitation of the  $^{12}\text{C}^*$  (4.44 MeV) and  $^{16}\text{O}^*$  (6.13 MeV) are clearly visible.

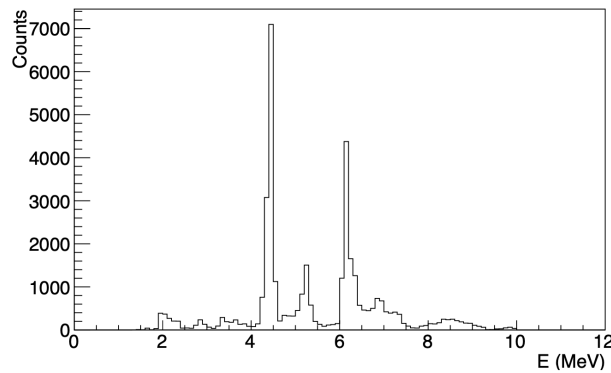


**Figure 4.2.** Energy spectrum of PG, simulated with a 160 MeV proton beam impinging on PMMA.

The simulated detector materials are defined using the correct chemical composition and density. The only exception is the ALPIDE electronic board which

was simulated by a  $100\mu\text{m}$  kapton layer and a  $50\mu\text{m}$  aluminium layer, to obtain the equivalent material budget. The simulations performed exploit some customized user routines in order to built an output data-set, containing the particle fundamental information, as position and momentum at generation, death and crossing of different regions, energy, momentum and position at crossing regions and also the energy released in the different constituents of the detectors. In the simulation used for this studies all the events are registered.

## 4.2 Trigger strategies and background analysis

As in the events of interest the lepton pair deposits some energy both in the converter and in the calorimeter, the natural choice is to built a time coincidence between the signals coming from the two detectors. The coincidence time window could be easily tuned in the concentrator board. In the following paragraph the expected signal in the mentioned detectors is shown.

### 4.2.1 Study of the event topology

At the beginning, the detectors expected response was studied considering all the simulated events. In Figure 4.3 and Figure 4.5 the distribution of the energy deposited in the calorimeter and in the converter are shown respectively. Then the detector response was studied considering only the events of interest, i.e. considering only the events in which a pair generated in the converter crosses the planes of the tracker and reaches the calorimeter. In Figure 4.4 and Figure 4.6 the distribution of the energy deposited in the calorimeter and in the converter are shown respectively considering only the events of interest. From now on we will call "*General case*" the case in which all the events are considered, and "*Pair case*" the case in which only the events in which a pair generated in the converter reaches the calorimeter, are considered.

The fraction of the events in which a gamma produce an  $e^+ e^-$  pair while both the leptons interact in the calorimeter is  $\approx 10^{-4}$ . From Figure 4.3 and Figure 4.4 it can be seen that for the events of interest the energy release in the calorimeter is for the most part less than 10 MeV. Furthermore, looking at the energy released in the converter by the signal, it is observed that it is for the most part less than 4MeV. ~~These observations are also confirmed by the plot of the energy released in the calorimeter as a function of the energy released in the converter~~ Figure 4.7. The two bands in Figure 4.7 are mainly due to secondary protons (it will be shown in Figure 4.15): the band between 10MeV and 20MeV are the protons that stop in the calorimeter, while the band between 5MeV and 10MeV are those that come out from the calorimeter.

It has to be also observed that the photons can also interact by Compton effect, producing an electron of the order of few MeV (Figure 3.3) that releases a similar energy both in the converter and in the calorimeter. As in this case just one electron would be absorbed by the calorimeter, the number of the activated calorimeter pixel is expected to be smaller with respect to the pair case. In Figure 4.8 and Figure 4.10 the number of activated pixels in the calorimeter and in the converter are shown respectively for general case, while in Figure 4.9 and Figure 4.11 the same quantities are shown for the pair case. As can be observed the signal of interest is associated with at least 2 activated pixels. It can also be observed that the number of activated pixels in the calorimeter by the signal is on average 4, this is reasonable considering

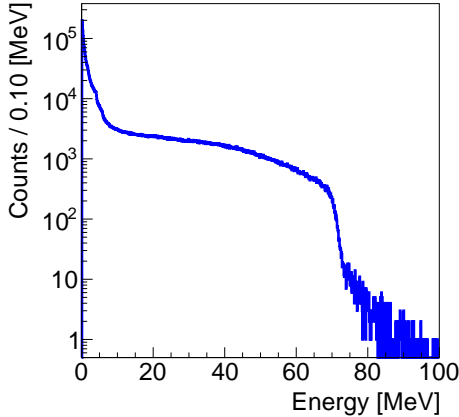


**Figure 4.3.** Spectrum of the energy released in the calorimeter, considering all the events (in log scale).

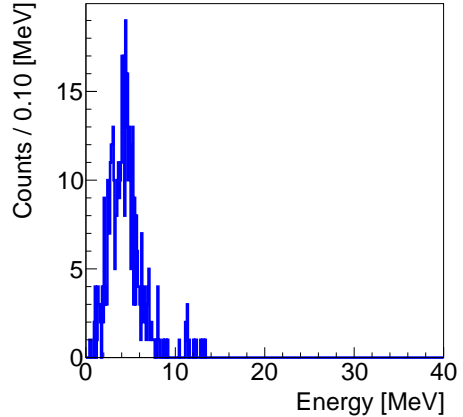


**Figure 4.4.** Spectrum of the energy released in the calorimeter, considering only the events of interest.

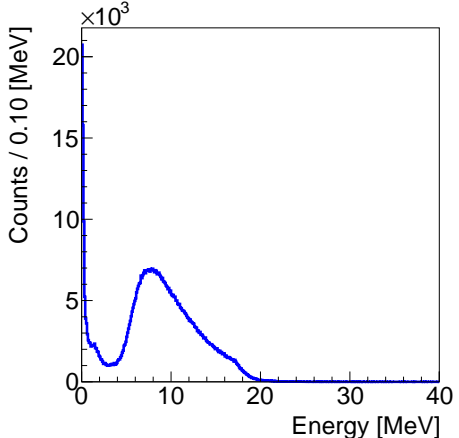


**Figure 4.5.** Spectrum of the energy released in the converter, considering all the events.

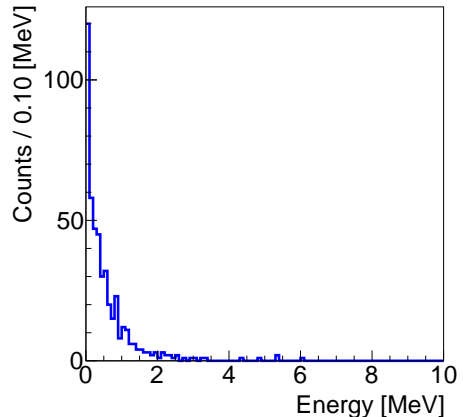


**Figure 4.6.** Spectrum of the energy released in the converter, considering only the events of interest.

that the leptons can travel in the calorimeter on average a greater distance than the size of a calorimeter pixel. Therefore the plots in Figure 4.3, Figure 4.5, in Figure 4.4, Figure 4.6, Figure 4.8, Figure 4.9, Figure 4.11, Figure 4.10 suggest that an effective trigger selection, capable to reject the main background sources, could be made requiring more than one activated pixel in the calorimeter and an upper threshold on the energy released in the converter and in the calorimeter.

However, the current architecture of the read-out system does not allow to built a majority, i.e. the coincidence of two or more single channels, as those are not accessible. As describes in subsection 3.2.4, the BASIC provides only a trigger signal which is asserted when at least one channel overcomes the set threshold. Moreover, it is not possible to set an upper threshold on the total signal, but just a lower threshold on the single channel.

Therefore the coincidence between the calorimeter and converter could be asserted

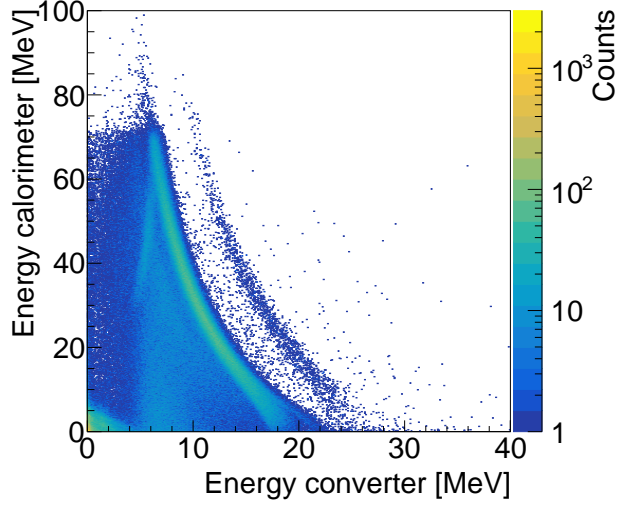


**Figure 4.7.** Energy released in the calorimeter as a function of the energy released in the converter.

when at least one channel of both detectors is over threshold. By the way, after the ASIC read-out procedure it would be possible to implement in the concentrator firmware a second level trigger which exploits the number of activated pixels and the total energy released in the devices. In this case an additional dead time of the order of few tens of microsecond due to the ASIC read-out procedure has to be considered.

Now two important quantities are introduced, useful in determining whether a trigger strategy is effective or not.

- **Efficiency:** it indicates among all the signal events how many are selected, and it is defined as the ratio between the selected events that are true  $N_{sel,true}$  and all the true events  $N_{true,all}$  (Equation 4.1).

$$\epsilon = \frac{N_{sel,true}}{N_{true,all}} \quad (4.1)$$

- **Purity:** it indicates among all the selected events how many are signal events and it is defined as the ratio between the selected events that are true  $N_{sel,true}$  and all the selected events  $N_{sel,all}$  (Equation 4.2).

$$p = \frac{N_{sel,true}}{N_{sel,all}} \quad (4.2)$$

In following paragraphs the efficiency and purity will be evaluated as a function of the threshold set in the energy released in the calorimeter and in the converter. However, in the preliminary tests, the performance of the PAPRICA chamber will be measured using converters of different passive materials, aiming to find the best compromise in terms of pair production cross-section, and impact of the nuclear recoil and MS. For this reason, I also evaluated the possibility to implement a trigger that exploits only the calorimeter signals.

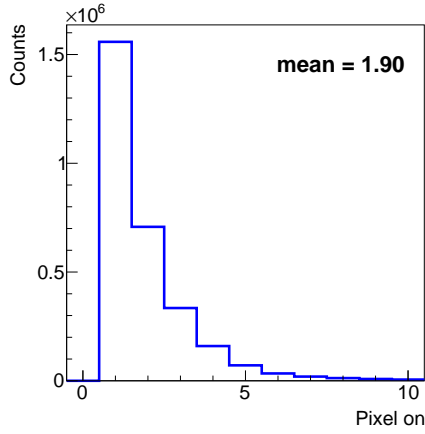


**Figure 4.8.** Number of activated pixels in the calorimeter, considering all the events.

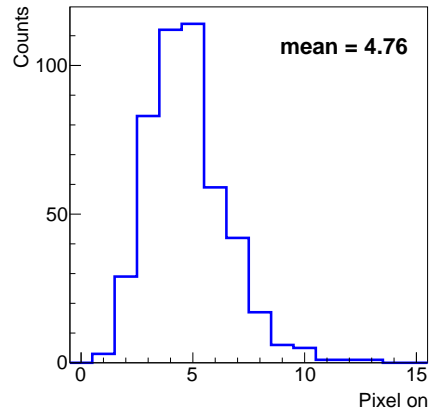


**Figure 4.9.** Number of activated pixels in the calorimeter, considering only the events of interest.

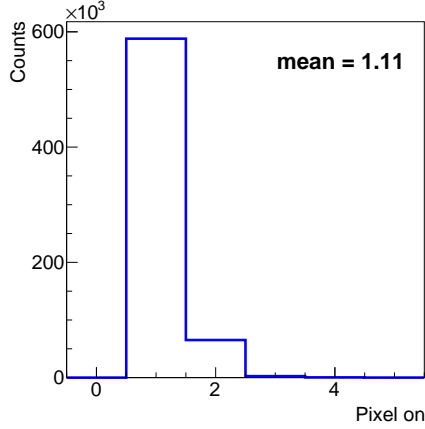


**Figure 4.10.** Number of activated pixels in the converter, considering all the events.

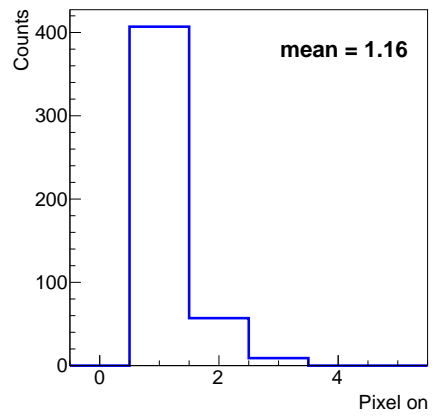


**Figure 4.11.** Number of activated pixels in the converter, considering only the events of interest.

#### 4.2.2 Trigger using calorimeter in coincidence with converter

Initially I evaluated the efficiency and purity of a first level trigger, as a function of the threshold on the calorimeter channels while fixing a 100 keV threshold on the converter channels. The plots of efficiency and purity as a function of the threshold per pixel in energy considering a first level trigger are shown in Figure 4.12.

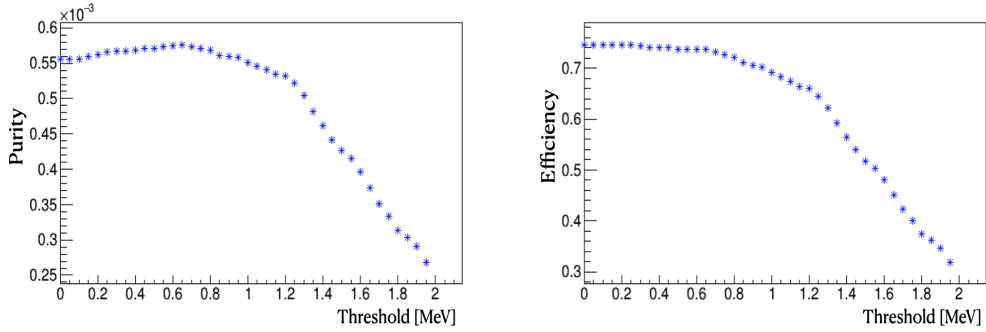


**Figure 4.12.** Purity vs threshold per pixel in energy (left) and efficiency vs threshold per pixel in energy (right), using converter as trigger and considering at least 1 pixel on.

To have a good efficiency ( $\approx 70\%$ ) the threshold has to be kept under 1 MeV, at expense of a very low purity ( $10^{-4}$ ).

With such kind of trigger, at therapeutic beam intensity of  $10^{10}$ , the rate of events able to arm the trigger would be of the order of  $10^6 s^{-1}$ . When including the detector dead time of  $100 \mu s$ , as measured by previous tests, it means that the trigger rate is saturated at 10 kHz and the resulting rate of events of interest is very low, about 1 Hz. Moreover for this trigger strategy the background is dominated by the secondary protons crossing the converter and entering in the calorimeter ( $\approx 89\%$ ) and by the photons interacting Compton in the converter ( $\approx 4\%$ ). Therefore the implementation of a second level trigger is really crucial to allow a test with therapeutic beams.

As a first step, I evaluated the impact of selecting the events according to the expected number of pixels activated in the calorimeter. In order to do this, I studied the occupancy (number of pixels on) as a function of the per-pixel threshold for the two cases: general case and pair case, shown in Figure 4.13.

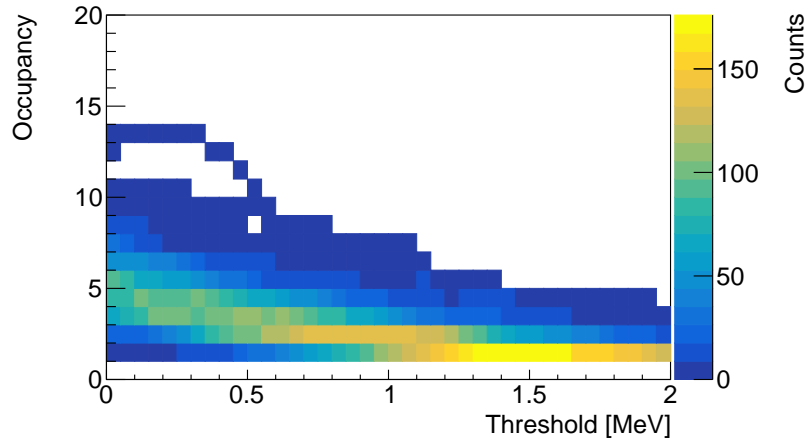


**Figure 4.13.** Occupancy vs threshold per pixel in energy for pair case, using converter as trigger. The threshold has been varied from 0 to 2 MeV every 50keV.

From Figure 4.13 I extracted the efficiency and purity as a function of the threshold per pixel in energy.

I have studied the number of activated pixels above a certain threshold in energy per pixel in pair case (Figure 4.13). As expected the higher the threshold per pixel, the fewer activated pixels above that threshold.

The minimum energy released in the calorimeter is about 1 MeV (Figure 4.4) and the minimum number of pixels in pair case is 2, so I tried to study what happens by varying the calorimeter energy threshold while fixing the converter threshold at 100 keV having two or three activated pixels.

So the efficiency and purity calculation was done considering the events in which at least 2 or 3 pixels are turned on. The plot of efficiency and purity as a function of the threshold considering converter as trigger are shown in Figure 4.14. For the calculation the Equation 4.1 and Equation 4.2 are used.

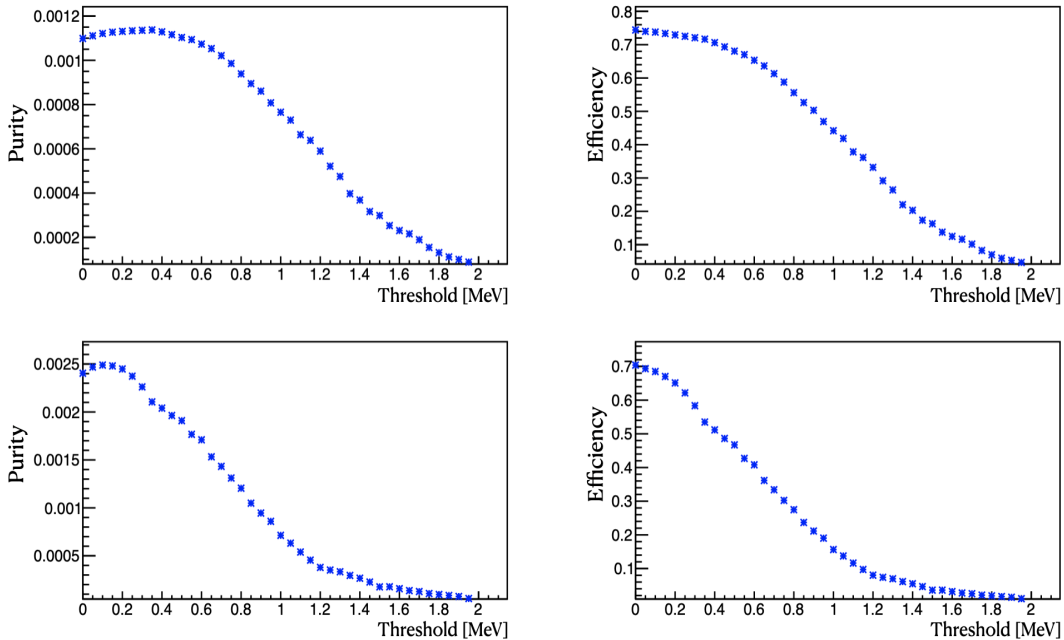


**Figure 4.14.** On the top purity vs threshold per pixel in energy (left) and efficiency vs threshold per pixel in energy (right), using converter as trigger and considering at least 2 pixels on. On the bottom the same considering 3 pixels on. The threshold has been varied from 0 to 2 Mev every 50keV.

On the top of Figure 4.14 at least 2 activated pixels are considered. It can be noted a slightly decreasing before 500keV, where the efficiency is grater than 70% and the purity is  $10^{-3}$ , and then a drop follows. On the bottom of Figure 4.14 3 activated pixels are considered. In this case the efficiency decreases more rapidly with the threshold, but the purity does not change significantly.

From Figure 4.14 it can be noted that in order to maximize the efficiency and purity values it is appropriate to choose a threshold per pixel in energy below 500keV.

Using the MC truth registered in the output of the FLUKA simulations, I separated the different background contributions. I distinguished the following kind of events:

- secondary protons that cross the converter and enter in the calorimeter
- neutrons that cross the converter and enter in the calorimeter

- delta-rays that cross the converter and enter in the calorimeter
- events in which a particle crosses the converter but, before entering in the calorimeter, interacts changing its nature. This are what we call "mixed events"
- gamma which interacts by Compton effect in the converter, producing an electron that enters in the calorimeter
- gamma which interacts by photoelectric effect in the converter, producing an electron capable to reach the calorimeter.

Such study has been carried on requiring a threshold on the energy released in the converter at 100keV, a threshold on the energy released in the calorimeter and at least 2 pixel on. The Table 4.1 shows the percentage of events for each background sources with respect to the number of trigger events. In the table it is also shown the contribution of the pair signal.

Background	Number of events (%)
<b>protons</b>	88,9
<b>neutrons</b>	0,9
<b>electrons</b>	1,08
<b>mixed events</b>	1,5
<b>Photoelectric converter</b>	1,6
<b>Compton converter</b>	4,5
<b>Pair Signal</b>	0,2

**Table 4.1.** Background contributions considering energy released in the converter grater than 100 keV and energy released in the calorimeter with 2 pixel on at 500keV.

The Table 4.1 shows that the main contribution to the background is constituted by the proton interactions ( $\approx 89\%$ ) and by the photons interacting Compton in the converter ( $\approx 4.5\%$ ).

In Figure 4.15 the energy released in the converter is shown for protons, neutrons and electrons, using converter as trigger. From Figure 4.15 it is shown that neutrons and electrons have a low energy release in the converter, mostly less than 4 MeV.

In order to reduce the protons contributions I study the impact on the purity and efficiency by requiring a total energy released in the converter lower than 4 MeV and in the calorimeter lower than 10 MeV.

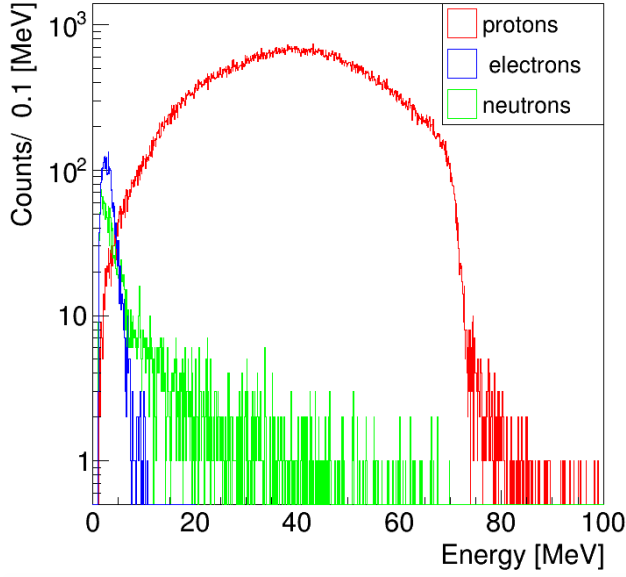


**Figure 4.15.** Energy released in the converter by protons (red), electrons(blue) and neutrons (green) (in log scale).

In Figure 4.16 plots of occupancy as a function of threshold per pixel in energy are shown, considering a trigger where the converter is in coincidence with the calorimeter and in which  $100\text{keV} < E_{conv} \leq 4\text{MeV}$  and  $E_{calo} \leq 10\text{MeV}$ .

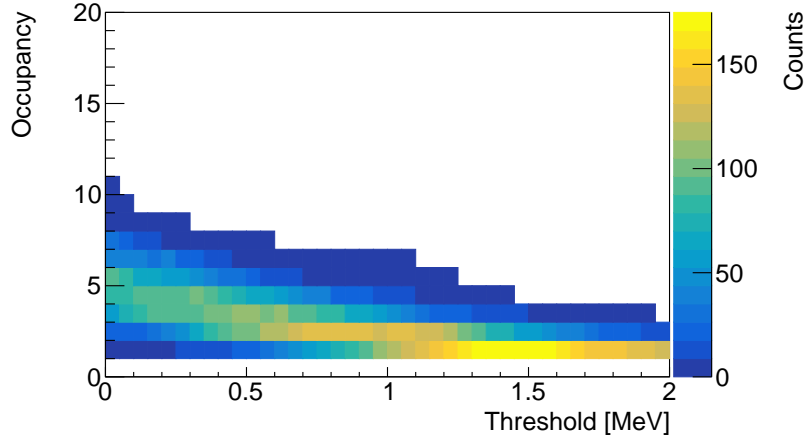


**Figure 4.16.** Occupancy vs threshold per pixel in energy for pair case, considering  $100\text{keV} < E_{conv} \leq 4\text{MeV}$  and  $E_{calo} \leq 10\text{MeV}$ . The threshold has been varied from 0 to 2 MeV every 50keV.

The efficiency and purity were calculated as a function of the threshold per pixel in energy. This calculation is made considering at least 2 or 3 pixels turned on. The plot of efficiency and purity for this trigger system are shown in Figure 4.17.

From Figure 4.17 it can be noted that in order to maximize the efficiency and purity values it is appropriate to choose a threshold per pixel in energy of  $\approx 500\text{keV}$ .

It is possible compare this results with those obtained using the previous trigger strategy and it can be noted that the efficiency remains almost the same, while the

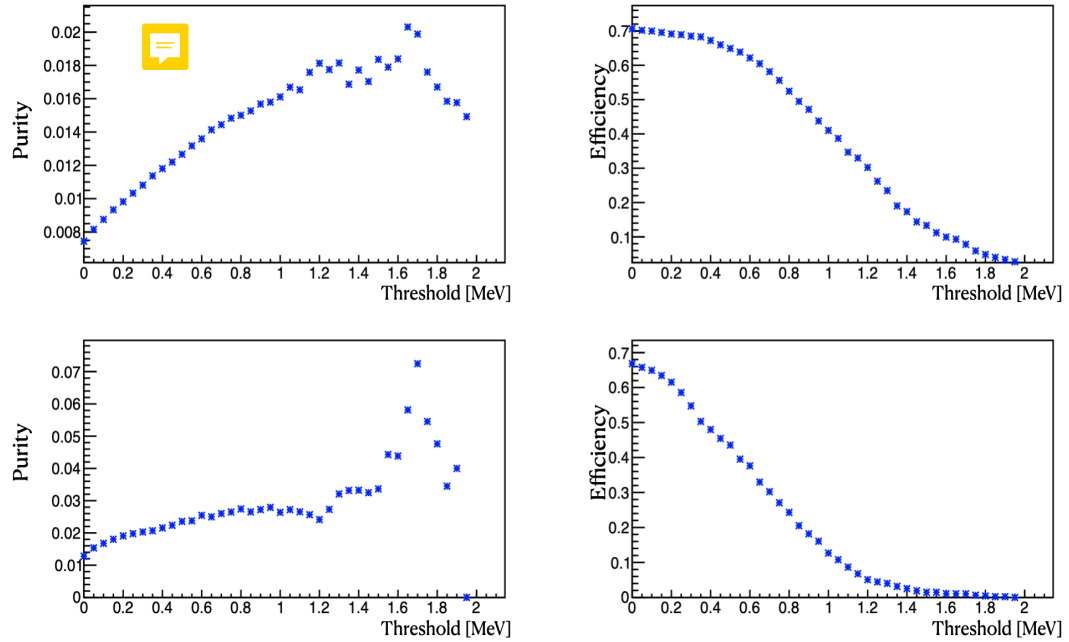


**Figure 4.17.** On the top purity vs threshold per pixel in energy (left) and efficiency vs threshold per pixel in energy (right), considering  $100\text{keV} < E_{\text{conv}} \leq 4\text{MeV}$  and  $E_{\text{calo}} \leq 10\text{MeV}$  and considering at least 2 pixels on. On the bottom the same considering 3 pixels on. The threshold has been varied from 0 to 2 Mev every 50keV.

purity improves significantly from the order of  $10^{-3}$  to  $10^{-2}$ . Moreover comparing this results with the one obtained considering a first level trigger it can be seen that the purity improves by a factor 100, from  $10^{-4}$  to  $10^{-2}$ . Moreover with a dead time of  $100\mu\text{s}$  a trigger rate of  $\approx 9.9$  kHz and a rate of events of interest of  $\approx 150$  Hz are expected.

As mentioned the threshold at 100keV on the energy released in the converter was chosen reasonably low. In order to investigate whether the choice of the lower threshold affected the analysis, the efficiency as a function of the lower threshold in the converter was studied (Figure 4.18). From Figure 4.18 it can be seen that the efficiency varies with the threshold in the converter. The efficiency is  $\approx 70\%$  with a threshold of 100keV and  $\approx 30\%$  with a threshold of 500keV. This plot shows the importance of choosing a suitable threshold in the converter.

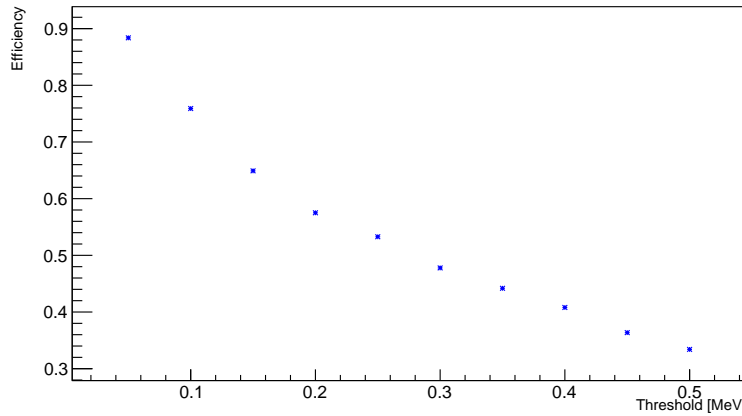


**Figure 4.18.** Efficiency as a function of the energy threshold in the converter. The threshold has been varied from 0.5keV to 500keV every 0.5 keV.

Also in this case it is presented an analysis of the different background sources. In Table 4.2 the background contributions for the second trigger strategy ( $100\text{keV} < E_{conv} \leq 4\text{MeV}$  and  $E_{calo} \leq 10\text{MeV}$  and 2 pixel on at 500keV) are studied.

Background	Number of events (%)
protons	0,5
neutrons	7,4
electrons	11,4
mixed events	15,9
Photoelectric converter	15,8
Compton converter	46,5
Pair Signal	1,5

**Table 4.2.** Background contributions for  $100\text{keV} < E_{conv} \leq 4\text{MeV}$  and  $E_{calo} \leq 10\text{MeV}$  and 2 pixel on at 500keV.

Let's compare the background tables for this trigger strategies. It can be observed that the contribution of the proton is significantly reduced ( $\approx 0.5\%$ ).

However, an unavoidable contribution due to secondary neutrons and electrons generated in Compton scattering of photons inside the converter, remains.

Mixed events contribute to the background in case of trigger with threshold on the total energy ( $\approx 16\%$ ).

The background due to the gamma is not modified by the trigger strategies, its contribution is smaller for the trigger without a threshold in the converter but becomes important in the other case. The greatest contribution is given by Compton events in the converter (up to  $\approx 46\%$  in the case of trigger with threshold both in the converter and in the calorimeter).

On the other hand the pair signal remains almost unchanged using the different trigger strategies, its contribution is also greater for the trigger with threshold both on converter and calorimeter ( $\approx 1.5\%$ ).

#### 4.2.3 Trigger using calorimeter information

The converter of PAPRICA detector is constituted by LYSO fibers. The choice of an active material allows for selecting the events using a coincidence signal occurs in the converter and in the calorimeter.

However, it is also possible to use a passive converter. The converter material may have an impact on the spatial resolution, as it affect the nuclear recoil and multiple scattering suffered by electrons produced in the detector volume. In this section I investigated the possibility to make a trigger using only the calorimeter signals.

Also in this case it was study the correlation between energy and occupancy for the two cases: general case and pair case. The efficiency and purity were calculated as a function of the threshold in energy per pixel, considering at least 2 or 3 pixels turned on and considering only the calorimeter information with an energy threshold  $E_{calo} \leq 10 MeV$  as trigger. The plot of efficiency and purity as a function of the threshold are shown in Figure 4.19.

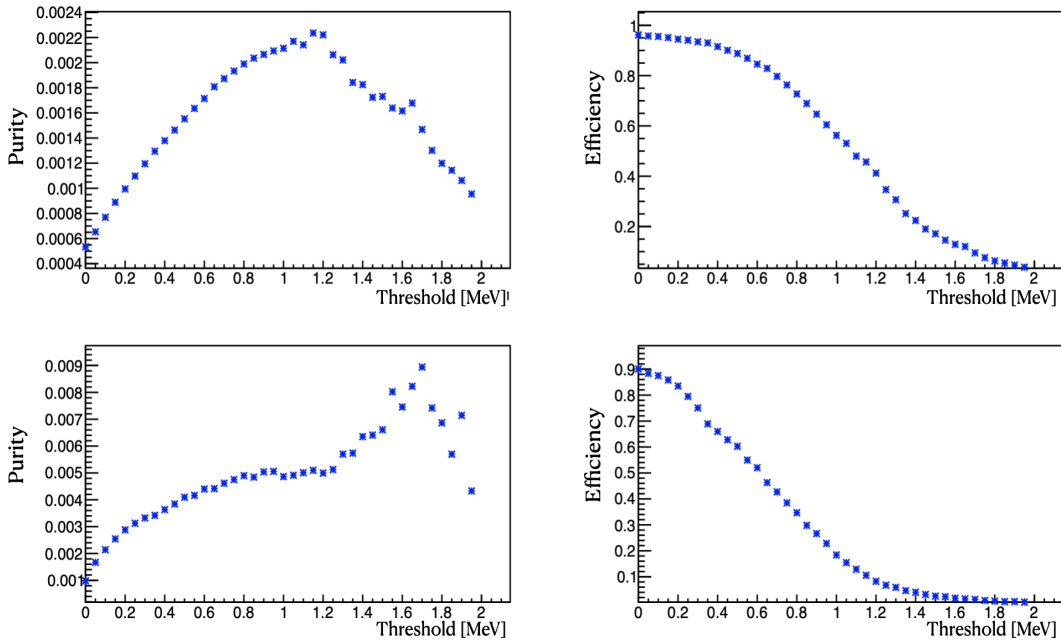


**Figure 4.19.** On the top purity vs threshold per pixel in energy (left) and efficiency vs threshold per pixel in energy (right), using calorimeter as trigger and considering at least 2 pixels on. On the bottom the same considering 3 pixels on. The threshold has been varied from 0 to 2 MeV every 50keV.

From Figure 4.19 it can be noted that the maximum efficiency is 90% compared to 70% of the previous cases that are due to the presence of the converter threshold. Moreover, to maintain efficiency values within 70%, a threshold less than 500 keV must be chosen, with a purity of the order of  $10^{-3}$ .

Finally the background was studied also in this case. This does not consider the converter but only the information of the calorimeter, so in this case the events that occur only in the calorimeter must be considered as background sources.

In Table 4.3 the background contributions for the last trigger strategy ( $E_{calo} \leq 10MeV$  and 2 pixel on at 500keV) are studied.

Background	Number of events (%)
protons	2,5
neutrons	36,8
electrons	4,3
Compton converter	4,9
Compton calo	48,3
Photoelectric converter	1,6
Photoelectric calo	0,07
Pair Signal	0,2

**Table 4.3.** Background contributions for  $E_{calo} \leq 10MeV$  and 2 pixel on at 500keV.

From Table 4.3 it can be seen that for this trigger strategy the background is mainly due to the events that interact by Compton effect in the calorimeter ( $\approx 48\%$ ) and to neutrons interactions ( $\approx 37\%$ ).

Also in this case the pair signal remains almost unchanged.

### 4.3 Expected trigger rate in a realistic scenario

From the analysis of the different trigger strategies it is possible to conclude that, in order to discriminate the background events, it is necessary to focus on the use of a trigger with the converter. The best trigger system is therefore the one in which the calorimeter is considered in coincidence with the converter.

Analysing the efficiency and purity for the proposed trigger strategies, it was highlighted that it is appropriate to set a threshold per pixel in energy  $E_{thr} = 500$  keV, and a threshold on the number of activated pixel of at least 2.

Analysing the different background contributions with the different trigger strategies, we suggest as a recommended trigger strategy the one in which an energy threshold is established in both the converter and the calorimeter. In particular  $100keV < E_{conv} \leq 4MeV$  and  $E_{calo} \leq 10MeV$  and 2 pixel on at 500keV. In this way it is possible to discriminate most of the background events and have a good contribution of signal events.

Therefore in order to develop this trigger logic a second level hardware trigger has to be implemented.

Furthermore, for the proposed trigger system, an analysis was carried out on the rates in order to optimize the dead time of the detector. Unlike other range monitoring techniques based on prompt-gamma imaging, PAPRICA has a better efficiency due to the fact that it exploits photons with energy more than 4MeV, for

which the cross-section of PP becomes important. But the impact of dead time must also be considered in order to evaluate how many events of interest can be measured.

To understand the impact of dead time for the chosen trigger strategy, the rate of measured events and signal events (events of interest) were calculated.

How to calculate the rate of measured events and interesting events is explained hereafter.

In our system there are  $10^7$  primary protons and the rate of primary protons is  $10^{10}$  protons/s. The rate of measured events can be calculated from Equation 4.3.

$$N = \frac{M}{1 - M\tau} \quad (4.3)$$

where  $M$  is the rate of measured events (what we want to calculate),  $\tau$  is the dead time and  $N$  is the theoretical rate (triggered events/s).

Setting a trigger system, knowing the theoretical rate value and fixed the dead time value, it is possible to calculate the rate of measured events. Multiplying this by the corresponding purity value it is possible to calculate the rate of events of interest.

Considering the trigger system such that  $100\text{keV} < E_{conv} \leq 4\text{MeV}$  and  $E_{calo} \leq 10\text{MeV}$  and 2 pixel on at 500keV, the rates of measured events and of interesting events were calculated for three different dead time values. The results are shown in Table 4.4.

Dead time	Rate of measured events (kHz)	Rate of good events (Hz)
$\tau=100\mu\text{s}$	9.99	149.36
$\tau=200\mu\text{s}$	4.99	74.69
$\tau=500\mu\text{s}$	1.99	29.88

**Table 4.4.** Rate studies for different dead time values, considering  $E_{conv} \leq 4\text{MeV}$  and  $E_{calo} \leq 10\text{MeV}$  and 2 pixel on at 500keV.

For this trigger strategy it was also calculated the ratio between the rate of interesting events and the rate of measured events (Equation 4.4).

$$R = \frac{\text{rate of interesting events}}{\text{rate of measured events}} \quad (4.4)$$

For the three dead time values the ratio does not change significantly, as the value of the ratio is  $R \approx 1.5\%$  for all the three values of dead time. These calculations can also be repeated in the case of trigger without energy threshold and 2 pixel on at 500keV, getting a ratio  $R \approx 0.15\%$ , for all the three dead time values. This further demonstrates that in order to have a good rate of interesting events and to optimize the dead time it is better to use a trigger system in which the converter is in coincidence with the calorimeter, both with an energy threshold.

## Chapter 5

# Reconstruction of the prompt-gamma emission profile

The aim of PAPRICA is to reconstruct the emission profile along the beam axis of the prompt-gamma produced during a PT treatment. In this chapter the reconstruction algorithm that leads to the gamma emission point is described, discussing the performance and limitations of the technique in the context of range monitoring application.

## 5.1 Reconstruction algorithm

In order to image the PG emission distribution, the incoming direction of the PG impinging on the converter and creating the electron-positron pair is reconstructed in three steps: reconstruction of the leptons production vertex, photon direction measurement and photon emission position reconstruction.

### 5.1.1 Photon direction

The photon momentum is computed from the momentum conservation in Pair Production, neglecting the nucleus recoil, as in Equation 5.1. The nucleus recoil is a not-accessible parameter and consequently can be neglected, introducing an intrinsic limit in PG production point reconstruction.

$$\hat{\mathbf{p}}_{reco}^{\gamma} = \mathbf{p}^+ + \mathbf{p}^- \quad (5.1)$$

Equation 5.1 can be written by separating the modulus and the direction of particle and gamma momentum, as in Equation 5.2

$$\hat{\mathbf{p}}_{reco}^{\gamma} = \frac{p^-}{p_{reco}^{\gamma}} \hat{\mathbf{p}}^- + \frac{p^+}{p_{reco}^{\gamma}} \hat{\mathbf{p}}^+ \quad (5.2)$$

Therefore the direction of the photon is given by the weighted sum of the electron and positron directions, where the weight is given by the fraction of the photon momentum acquired by each particle.

### 5.1.2 Track identification and selection

In order to explain the MC simulation used for our reconstruction studies, the concept of detector hit has to be introduced: a hit is defined as the energy release

by one or more particles within an active detector (LYSO fiber, MAPS Si pixel, plastic scintillator pixels), that is above the detector energy threshold ( $E_{thr}$ ). As previously mentioned  $E_{thr} = 500$  keV has been chosen for the calorimeter pixels in order to optimize the trigger efficiency reducing the background contributions, while ~~no energy threshold has been set for the LYSO fibers and MAPS~~.

~~From now on the events of interest, defined as the events where a photon produces in the converter an electron-positron pair intercepting the calorimeter, will be selected applying a two level trigger strategy.~~ First, the hardware-like trigger studied in the previous section ( $100\text{keV} < E_{conv} \leq 4\text{MeV}$  and  $E_{calo} \leq 10\text{MeV}$ ) is implemented at the simulation level, asking for the presence of at least one converter hit and at least 2 calorimeter pixels over threshold ( $E_{thr} = 500$  keV). Then, a further selection has been applied asking for the presence of at least 2 hits in each tracker plane, as two leptons are expected crossing the calorimeter. Such request allows for rejecting most of the background, obtaining an event sample with ~~efficiency~~ of  $\approx 80\%$ .

The resulting trigger efficiency, defined as the ratio between the triggered events of interest with respect to the whole events of interest, is of the order of  $\approx 93\%$ .

~~A reconstruction algorithm has been developed in order to identify the leptons tracks, evaluate their direction and finally reconstruct the production vertex in the converter as the Point Of Closest Approach (POCA) between the tracks direction.~~

~~First of all when a lepton crosses the tracker, the adjacent hits in the tracker planes are grouped in clusters. A cluster will have a position given by the arithmetic average of the single hits positions.~~

Then for each event selected with the strategy described above, the algorithm looks for a couple of tracks pointing to the converter. All the possible combinations of three clusters (one per plane) are considered as track candidates.

As shown in Figure 5.1, the angle  $\theta_{ab}$  between the first segment  $a$  (from  $c_1$  to  $c_2$ ) and the second segment  $b$  (from  $c_2$  to  $c_3$ ) is computed for each track candidate. Then, the direction defined by the segment connecting  $c_1$  and  $c_2$  is assigned to each candidate. The  $c_3$  point is not used in order to not include the contribution of multiple scattering suffered by particles in the second MAPS plane. Finally, the vertex candidate position and its distance  $d_{conv}$  from the converter plane are computed.

The best track pair is selected from the candidates as the couple of tracks ( $t_1$  and  $t_2$ ), not having clusters in common, that minimises the sum between their angles ( $\theta_{ab}^{t_1} + \theta_{ab}^{t_2}$ ) and  $d_{conv}$ .

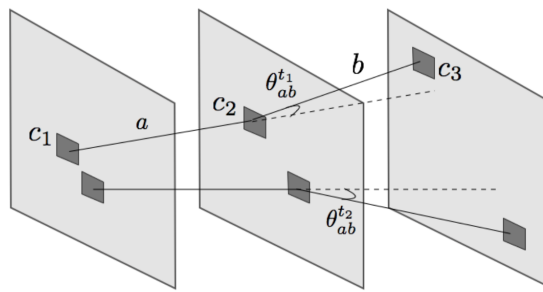


**Figure 5.1.** Sketch of the cluster assignment to a track in the reconstruction algorithm.

The MAPS plane are represented in light grey, while the clusters are highlighted in dark grey.  $c_1$ ,  $c_2$  and  $c_3$  belongs to track  $t_1$ .  $a$  and  $b$  are the segments between  $c_1 - c_2$  and  $c_2 - c_3$ , respectively. The angle  $\theta^{t_1}$  is reported, as well as for the second track  $t_2$ .

### 5.1.3 Lepton kinetic energy

In order to reconstruct the prompt photon emission position, the photon momentum has been computed according to subsection 5.1.1. The leptons momentum is evaluated exploiting the energy released in the calorimeter.

Therefore after detecting two tracks in the tracking system, one or more activated pixels of the calorimeter must be associated to each track in order to estimate the leptons momentum and reconstruct the photon direction. To this aim, the vector that joins the hits of the second and third plane is projected on the surface of the calorimeter.

Figure 5.2 shows the distance between the impact point of the lepton in the calorimeter and pixels associated to the lepton. This distribution allows to define a distance cutoff  $d_{cutoff} = 1.5$  cm between the projection of a track and the pixels that can be associated to it.

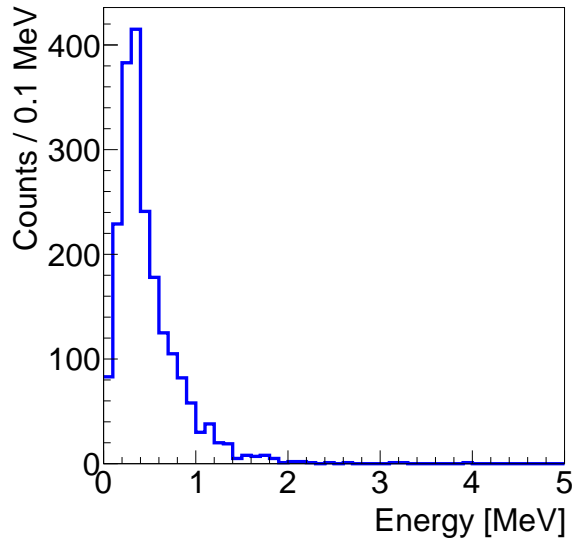


**Figure 5.2.** Distance between the impact point of the lepton in the calorimeter and pixels associated to the lepton.

Then for each hit a circle is drawn around its center and with radius  $d_{cutoff}$ . If there is a projection of a track inside the circle the pixel is associated to it and the deposited energy in the pixels associated to each track is added. If there are several projections the pixel is associated to the track with the closest projection (Figure 5.3).

Once the particle incoming direction on the converter plane has been calculated, the gamma emission position has been evaluated as the POCA between the nominal beam axis (the z axis in our simulated setup geometry) and the reconstructed particle direction.

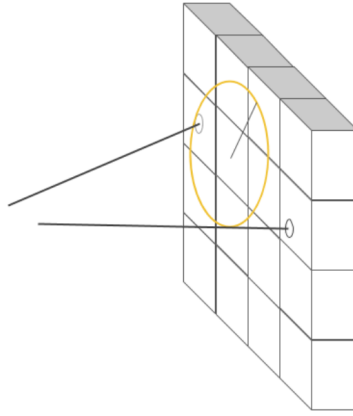


**Figure 5.3.** Projection of the tracks on the calorimeter, drawing a circular area of 1.5 cm radius around each activated pixel and assigning the pixel deposited energy to the track with the closest projection inside the area.

#### 5.1.4 Vertex

The pair production position is the generation point of electron and positron and consequently, in the vacuum, it is the vertex where their linear trajectories meet. In the real case, the multiple scattering in the converter and inside the three HICs of ALPIDE changes the particle direction and the lines defined by their momentum do not have an intersection point in the three-dimensional space. A good approximation of the vertex position is the Point Of Closest Approach (POCA), found as the midpoint of the Distance Of Closest Approach (DOCA). Consider two lines  $P(s)$  and  $Q(t)$ , in the parametric form the straight lines are defined by a point  $P_0, Q_0$  and a vector  $\mathbf{u}, \mathbf{v}$  respectively, as in Equation 5.3.

$$P(s) = P_0 + s\mathbf{u} \quad Q(t) = Q_0 + t\mathbf{v} \quad (5.3)$$

Let  $\mathbf{w}(s, t) = P(s) - Q(t)$  be a vector between points on the two lines, the goal is to find the parameters  $s_C$  and  $t_C$  that minimize the  $\mathbf{w}$  length.

In any n-dimensional space, the two lines are closest at unique points  $P_C = P(s_C)$  and  $Q_C = Q(t_C)$  for which  $\mathbf{w}(s_C, t_C)$  is the unique minimum for  $\mathbf{w}(s, t)$ . Further, if the lines are not parallel and do not intersect each other, then DOCA is defined by the segment  $P_C Q_C$ , joining these points, simultaneously perpendicular to both lines (Figure 5.4). That is, the vector  $\mathbf{w}_C = \mathbf{w}(s_C, t_C)$  is perpendicular to the line direction vectors  $\mathbf{u}$  and  $\mathbf{v}$ , and this is equivalent to it satisfying the two equations in 5.4.

$$\mathbf{u} \cdot \mathbf{w}_C = 0 \quad \mathbf{v} \cdot \mathbf{w}_C = 0 \quad (5.4)$$

These two equations may be solved by substituting  $\mathbf{w}_C = P(s_C) - Q(t_C) = \mathbf{w}_0 + s_C \mathbf{u} - t_C \mathbf{v}$ , where  $\mathbf{w}_0 = P_0 - Q_0$ , to get the two simultaneous linear equations in 5.5.

$$(\mathbf{u} \cdot \mathbf{u})s_C - (\mathbf{u} \cdot \mathbf{v})t_C = -\mathbf{u} \cdot \mathbf{w}_0 \quad (\mathbf{v} \cdot \mathbf{u})s_C - (\mathbf{v} \cdot \mathbf{v})t_C = -\mathbf{v} \cdot \mathbf{w}_0 \quad (5.5)$$

Defining the following parameters:  $a = \mathbf{u} \cdot \mathbf{u}$ ,  $b = \mathbf{u} \cdot \mathbf{v}$ ,  $c = \mathbf{v} \cdot \mathbf{v}$ ,  $d = \mathbf{u} \cdot \mathbf{w}_0$ ,  $e = \mathbf{v} \cdot \mathbf{w}_0$  the minimum length of  $\mathbf{w}_C$  corresponds to 5.6

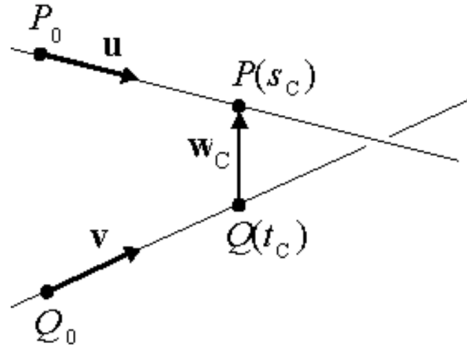


**Figure 5.4.** Minimum distance between lines.

$$s_C = \frac{be - cd}{ac - b^2} \quad t_C = \frac{ae - bd}{ac - b^2} \quad (5.6)$$

When  $ac - b^2 = 0$ , the two equations are dependant, the two lines are parallel, and the distance between the lines is constant. Otherwise the midpoint of segment defining the distance of closest approach, i.e. the best vertex approximation, may be found as Equation 5.7.

$$\text{POCA} = \frac{P(s_C) + Q(t_C)}{2} \quad (5.7)$$

The spatial resolution on the reconstructed vertex position has been evaluated in the case of the events of interest, computing the difference between the true and the reconstructed production vertex, it is shown in Figure 5.5. A resolution of  $\approx 2\text{mm}$  has been obtained for the vertex reconstruction on the YZ transverse plane. On the X axis, the vertex distribution is not symmetrical, with a standard deviation of  $\approx 5\text{mm}$ .

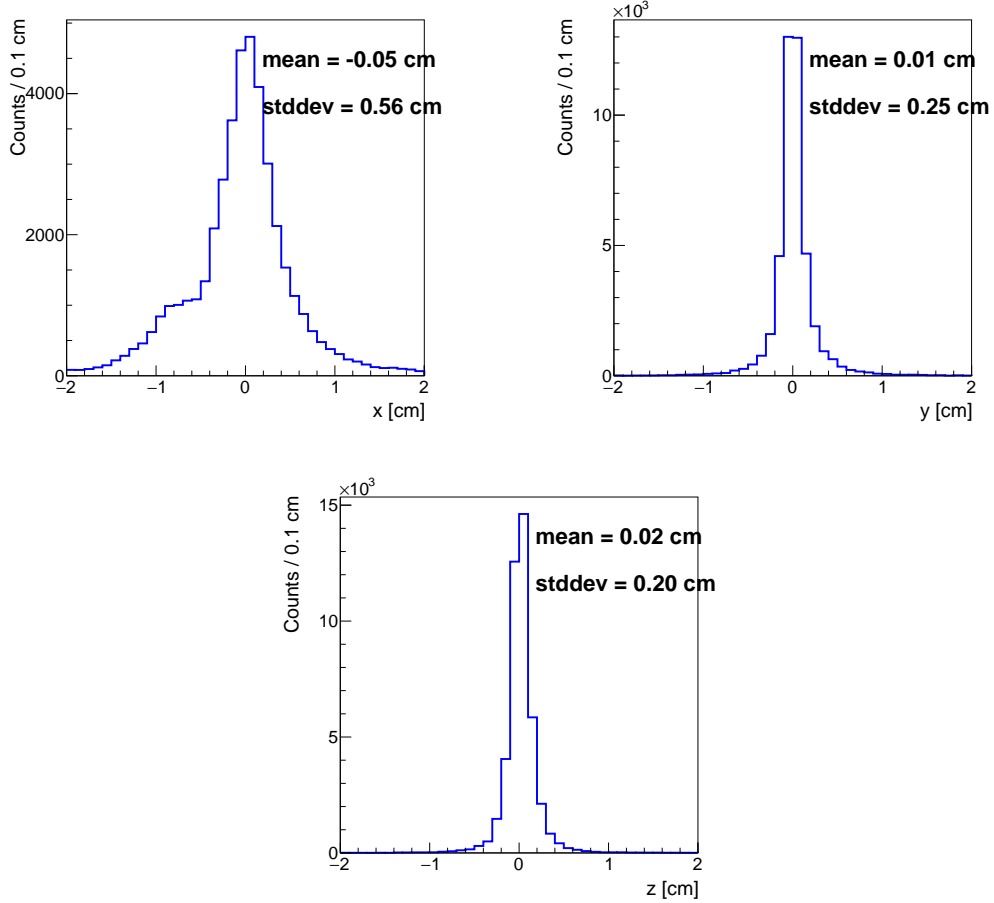


**Figure 5.5.** Resolution on the reconstructed vertex position along the x (left,top), y (right,top) and z (bottom) axes, considering only the events of interest.

### 5.1.5 Photon emission point

If the source distance from converter is known, the direction of the photon can be projected from the reconstructed vertex to a plane containing the source and parallel to the front side of the converter. Let define the gamma direction as:  $P(s) = P_0 + s\mathbf{u}$ . The plane containing the source may be individuated by a normal vector  $\mathbf{n}$  and a point Q. If  $\mathbf{n} \cdot \mathbf{u} = 0$ , the line is parallel to the plane and never intersects it. Otherwise the line intersects the plane in a unique point  $P(s_i)$  (Figure 5.6), which may be individuated requiring that the normal vector of the plane and the vector  $Q - P(s_i)$  are perpendicular, as in Equation 5.8

$$\mathbf{n} \cdot (Q - P(s_i)) = 0 \quad (5.8)$$

This is equivalent to Equation 5.9

$$\mathbf{n} \cdot (Q - P_0 - s_i\mathbf{u}) = 0 \quad (5.9)$$

with solution as in Equation 5.10

$$s_i = -\frac{\mathbf{n} \cdot (Q - P_0)}{\mathbf{n} \cdot \mathbf{u}} \quad (5.10)$$

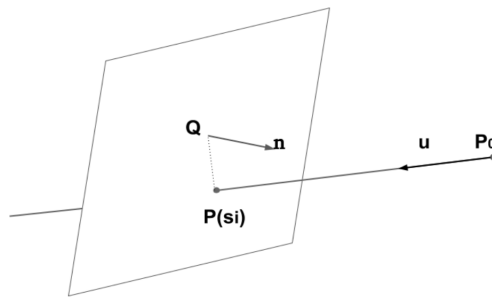


**Figure 5.6.** Intersection between a straight line and a plane

The reconstructed points on the source plane, one for each pair production event, are distributed around the source with a dispersion given by the angular resolution and the distance of the converter from the source. In fact, as can be deduced from simple geometric considerations, the distance between the source and the calculated emission point increases with the distance between the source and the chamber. The spatial distribution obtained may be analyzed, projecting the distribution on the axes of the plane.

## 5.2 Results

In Figure 5.7 the reconstructed PG emission profile along the beam axis is shown and compared with the actual emission profile at pair production, obtained exploiting the MC truth. Observing the reconstructed profile, a bias in the reconstructed position can be noticed, as the reconstructed position is systematically shifted towards the positive z axis. This artefact completely spoils the correlation between the fall-off of the gamma distribution and the Bragg peak depth, and has to be properly corrected. This item will be addressed in the following sections.

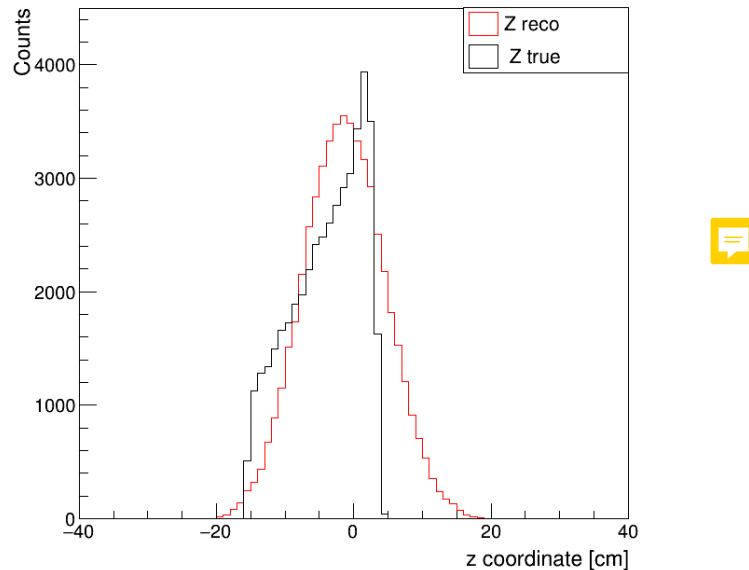


**Figure 5.7.** Reconstructed prompt photons emission distribution along the beam axis ( $z$  coordinate) (red). The distribution of the actual points production is superimposed (black).

### 5.2.1 Photon angular resolution

The angular resolution on the incoming photon direction is given by the convolution of several effects: neglect of the nucleus recoil, multiple scattering suffered by the electron inside the converter, resolution on the reconstructed vertex. The overall angular resolution has been assessed considering the angle  $\Delta\theta$  between the reconstructed direction of the photon and the true one given by the MC simulation, as defined in Equation 5.11.

$$\Delta\theta = \frac{\mathbf{p}_{\text{reco}}^\gamma \cdot \mathbf{p}_{\text{true}}^\gamma}{p_{\text{reco}}^\gamma p_{\text{true}}^\gamma} \quad (5.11)$$

The  $\Delta\theta$  distribution is shown in figure Figure 5.9. The angle  $\Delta\theta$  varies from event to event because it depends on the fraction of momentum of the photon given to the nucleus and on the stochastic events of the multiple scattering. The mean  $\Delta\theta$  is of the order of  $17^\circ$ .

The impact on the emission photon coordinate along the beam axis z is evaluated studying the plot shown in Figure 5.8. It shows the difference between the beam axis coordinate z profile of the PG emission point calculated using reconstructed momentum and the one calculated at leptons production. As a result of a Gaussian fit, a mean systematic error of  $\approx 2.5$  cm can be observed in the z reconstruction, while a statistical uncertainty of 6.5 cm has been obtained.

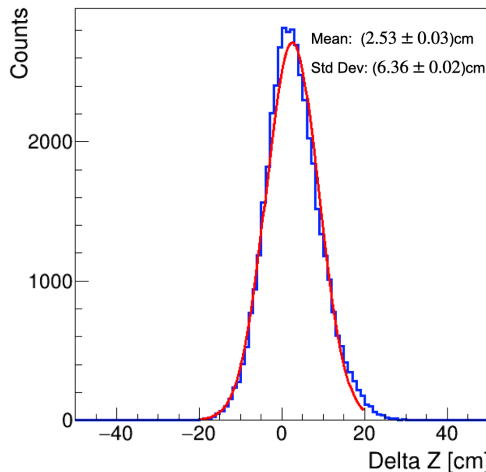


**Figure 5.8.** Difference between z profile of PG emission point calculated using reconstructed momentum and calculated at leptons production. A Gaussian fit was also made.

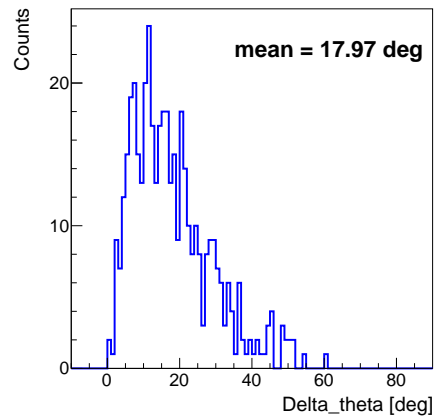


**Figure 5.9.** Angle distribution between true and reconstructed momentum.

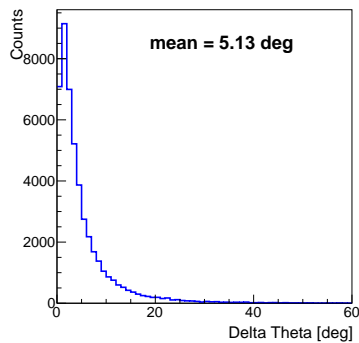
Under the assumption of no-bias, such resolution would be compatible with the clinical needs. In fact, identifying as a monitoring volume the distal part of a tumour  $1 \times 1 \times 0.2 \text{ cm}^3$ , 10 pencil beams are needed to target it, with a total number of primaries of  $\approx 10^{10}$ . In such application, envisaging a detector covering 2 sr (i.e. a factor  $\sim 20$  larger than the acceptance of PAPRICA in the described setup) a number of  $\sim 1000$  reconstructed tracks would be expected and therefore a resolution on the average value of the prompt photons emission position of  $\frac{6.3\text{cm}}{\sqrt{1000}} \approx 2\text{mm}$  could be obtained.

In order to dis-entangle the different contribution to the statistical uncertainty, I evaluated the following quantities.

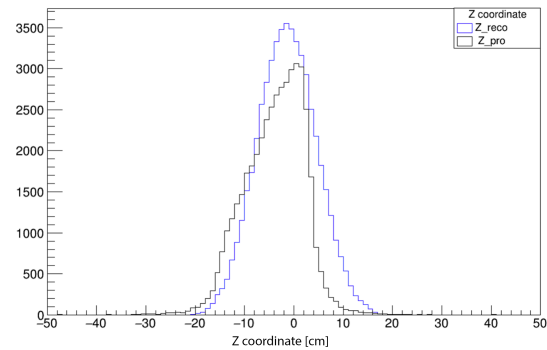
- $\Delta\theta_{pro}$ , defined as the angular difference of the reconstructed photon direction at pair production with respect to the true photon direction. This allows to evaluate the contribution on the photon reconstruction of the converter nuclear recoil.
- $\Delta\theta_{1plane}$ , defined as the angular difference of the incident leptons momentum at the entrance in the first tracker plane with respect to the true momentum. This allows to evaluate the impact of the multiple scattering suffered by the lepton pair crossing the tracker planes.

Figure 5.10 shows the  $\Delta\theta_{pro}$  distribution with an average value of  $\approx 5.1^\circ$ , while Figure 5.12 shows the  $\Delta\theta_{1plane}$  distribution and the obtained average value is  $\approx 17^\circ$ .

Figure 5.11 shows a comparison between two prompt-gamma emission profiles along the beam axis. One obtained calculating the momentum magnitude using the reconstructed energy and the other one obtained calculating the momentum magnitude at the instant of pair production.



**Figure 5.10.** Angular difference between the PG true momentum direction and the reconstructed momentum direction from electron and positron direction at the pair production.



**Figure 5.11.** Comparison between z coordinate profiles of the prompt-gamma emission point calculating the momentum magnitude from the reconstruction (blue) and at pair production (black).

In Figure 5.13 a comparison between the PG emission profiles along the beam axis is shown for two cases. The first is obtained using the reconstructed momentum, the second using the momentum magnitude calculated from the energy released by the particles crossing the first tracker plane.

In this case the contribution of the nucleus recoil and the multiple scattering suffered by the lepton pair in the converter is considered.

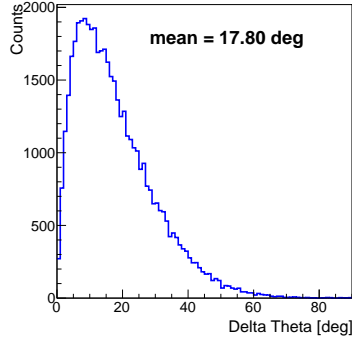


**Figure 5.12.** Angular difference between the PG true momentum direction and the reconstructed momentum direction using lepton momentum at the first tracker plane.

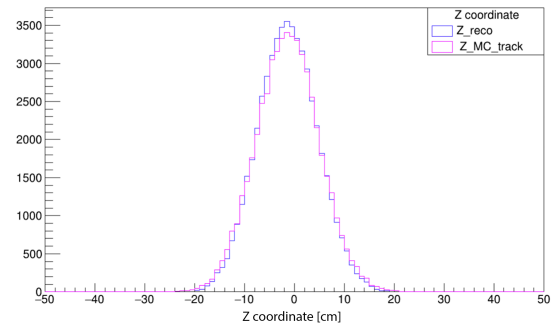


**Figure 5.13.** Comparison between z coordinate profiles of the prompt-gamma emission point calculating the momentum magnitude from the reconstruction (blue) and at first tracker plane (violet).

The z emission profile does not change significantly with respect to the reconstructed profile. Therefore the energy measurement strategy does not affect the reconstruction, which is instead dominated by multiple scattering and recoil effects in the converter. The spatial resolution of the order of 6 cm is due to the unavoidable contribution of the nucleus recoil in the kinematic reconstruction and to the multiple scattering suffered by the lepton pair within the converter.

### 5.2.2 Impact of energy measurement on spatial resolution

We compared two techniques for measuring kinetic energy. One associating the hits to the track, the kinetic energy associated to the track is the energy released in the associated hits. It is what we call "reconstructed energy ( $E_{reco}$ )". The other studying the type of particles associated to the tracks, the kinetic energy associated to the track is the kinetic energy of these particles when they cross the calorimeter. It is what we call "true energy ( $E_{true}$ )".

The plot of the difference between the energies calculated with these two techniques is shown in Figure 5.14, considering only the events of interest. A Gaussian fit is also made.

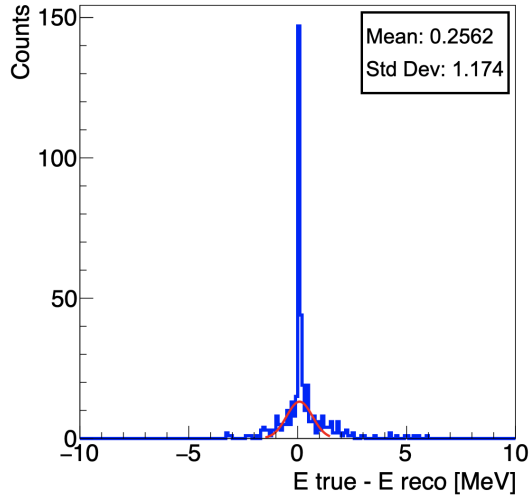


**Figure 5.14.**  $E_{true} - E_{reco}$  for a track considering only the events of interest, Gaussian fit is made.

From Figure 5.14 it can be observed that the energy released in the calorimeter is not equal to the energy at the entrance of the calorimeter. This is due to unavoidable energy losses due to physical effects such as leptons back-scattering and positrons annihilation. In this case we are not considering the resolution of the detector but we are only studying the MC results, then 5 % calorimeter resolution must be added.

Figure 5.15 shows the standard deviation of a Gaussian fit on the difference between the reconstructed PG emission profile along z and the one at the pair production, as a function of the reconstructed energy. The spatial resolution changes from a value of  $\approx 8\text{cm}$  with a photon energy of 2MeV to a value of  $\approx 5\text{cm}$  with a photon energy of 8MeV. Although the photon of 4 MeV using in PAPRICA system have the advantage to be the one more correlating to the Bragg peak higher energy photons have a better resolution.

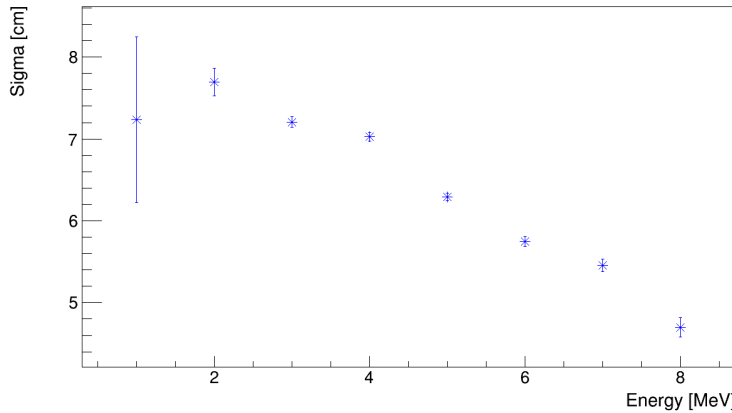


**Figure 5.15.** Standard deviation of a Gaussian fit on the difference between the reconstructed z profile and the z profile at the production as a function of the reconstructed energy. The energy has been varied from 0 to 10MeV every 1MeV.

In order to evaluate the impact of the leptons energy measurement on tracking three cases are studied where the lepton momentum magnitude is calculated in different ways:

- **Reconstruction:** momentum magnitude calculated using the reconstructed energy
- **Unitary:** momentum magnitude calculated using unitary energy
- **MC Calorimeter:** momentum magnitude calculated from the energy released by the particles entering in the calorimeter

Figure 5.16 shows a comparison between the PG emission profiles along the z axis for the three cases. The first is obtained using the reconstructed momentum, the second using unitary momentum and the last one using the momentum of the particles entering in the calorimeter.

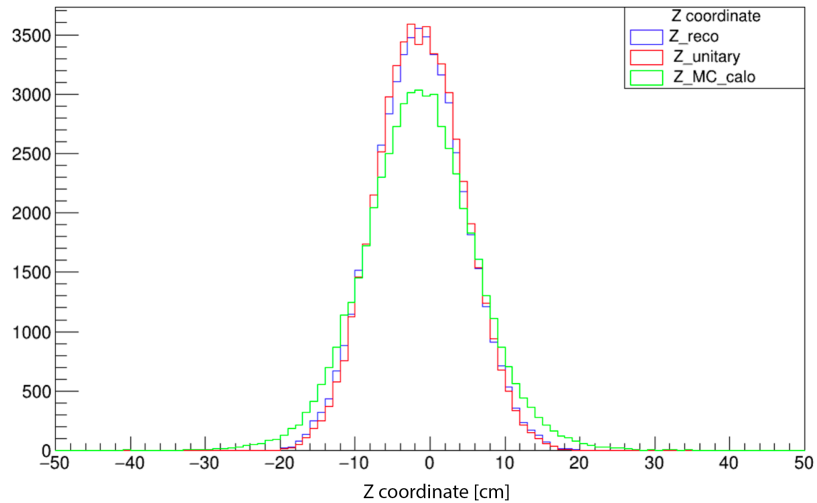


**Figure 5.16.** Comparison between z coordinate profiles of the prompt-gamma emission point for reconstruction (blue), unitary (red) and MC calorimeter (green) case.

From Figure 5.16 comparing the prompt-gamma emission profiles along the beam axis obtained with this energy measurement strategies it can be seen that the different measurement strategies do not affect significantly the reconstruction. It can be assert that the momentum measurement of the lepton does not affect significantly the calculation of reconstruction, however the presence of the calorimeter in the PAPRICA geometry is still mandatory to trigger the data acquisition and for the event selection.

### 5.2.3 Systematic error

In Figure 5.7 a systematic error in the reconstructed position is observed due to a geometrical effect arising as the photon angle with respect to the converter plane increases. This can be explain looking at Figure 5.17, where a scheme of the PG interaction in the converter is shown. The photon interaction vertex can be reconstructed with an angular resolution  $\Delta\theta$ , which is affected by multiple scattering within the converter plane. Therefore the PG emission profile along the beam axis will be shifted with respect to real vertex position. This will give rise to the observed bias. Such effect is a consequence of the large multiple scattering within the converter plane, and has to be corrected with an a posteriori MC-based calibration, as it will explain in the next section.

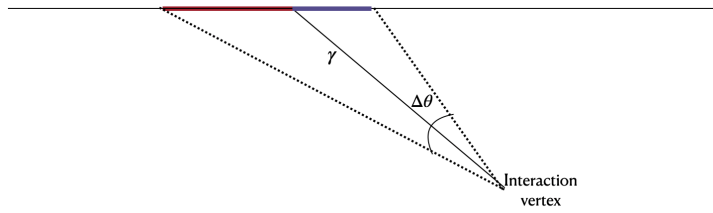


**Figure 5.17.** Scheme of the PG interaction in the converter, where  $\Delta\theta$  is the angular resolution. The PG emission profile along the beam axis will be shifted with respect to real vertex position.

### 5.3 Unfolding: a preliminary study

The systematic error made in the position reconstruction prevents to exploit the correlation between the Bragg peak and the fall-off of the PG distribution to monitor the beam range. Then, such effect must be corrected or calibrated. To this aim, in my thesis work, I implemented a preliminary method based on unfolding.

In particle physics measured distributions are different from the expectation for an ideal case because of the finite resolution and limited acceptance of the detectors. Unfolding is a statistical technique used to infer an unknown distribution  $f(t)$  for a variable  $t$  from the measured distribution  $g(s)$  of a variable  $s$  by using knowledge or assumptions on the probability distribution that links the observation to the “true” value. The distributions  $f(t)$  are often not directly accessible. The distribution  $g(s)$  of the measured variable  $s$  is related to the distribution  $f(t)$  by distortions and transformations. Using Monte Carlo methods the unfolding process from the actually measured distribution  $g(s)$  to the related true distribution  $f(t)$  can be simulated, although small changes in the measured distribution can cause large changes in the reconstructed true distribution.

The algorithm is implemented in the ROOT software as TUnfold package and has been tested on the FLUKA Monte Carlo simulation.

#### 5.3.1 Unfolding matrix

Since the bias in the photons reconstruction is only due to detector effects, in order to build the unfolding matrix, an ad-hoc simulation has been constructed: an extended photon source has been simulated inside a 80cm long PMMA target. The PMMA target sides have the same dimensions of the target used in the 160 MeV proton beam simulation (subsection 4.1.1). The source is uniform in  $z = [-40, 40]$  cm. The energy spectrum is the same shown in Figure 4.2. The photon source is generated isotropically. The PAPRICA detector is placed with the same geometry as in subsection 4.1.1. The choice of using an extended photon source is based on the assumption that the MC is well able to reproduce the photons transport and interaction, and therefore it is not dependent to the FLUKA MC nuclear cross section of the prompt photon production.

The unfolding matrix used in the algorithm is composed by (20x20) bins from [-20,20] on both axes. It is shown in Figure 5.18. The y axis is associated to the true  $z$  ( $z$  at production) while the x axis to the reconstructed  $z$ . The matrix elements are defined as the probability that a reconstructed track will be generated in a bin of the  $z$  coordinate at production and will be reconstructed in a bin of the reconstructed  $z$  coordinate. In the algorithm the tracks are selected with the trigger strategy described in subsection 5.1.2. If the two hits of the two chosen tracks on the first

tracker plane have the same father which is a photon the true  $z$  is saved. Else for the not reconstructed events a bin for  $z$  true is created in which an arbitrary value is saved. Therefore let  $i$  be a bin of  $z$  true and  $j$  a bin of  $z$  reconstructed each element of the matrix will contain a probability  $P_{ij}$  defined by the ratio between the number of events reconstructed in the  $j - bin$  and the number of true events in the  $i - bin$  that are reconstructed.

The configuration of the TUnfold algorithm has been optimised in order to minimise the differences of the unfolded spectrum with respect to the true one and the following parameters have been chosen: 20 bins for the unfolded final output starting from 20 measured bins, a regularisation strength  $\sim 0.01\text{--}0.02$ , with variations related to the different samples.

A study on binning will need to be done in future studies to assess systematic uncertainty.

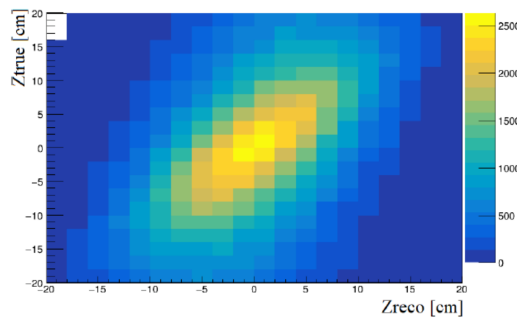


**Figure 5.18.** Unfolding matrix, Zreco is the reconstructed photon coordinate while Ztrue is the coordinate at pair production.

### 5.3.2 Bragg peak calibration

The purposes of my preliminary studies are: to obtain the reconstructed spectrum for proton beams at different energies, to apply the unfolding algorithm to the reconstructed spectra, to estimate the fall-off of the unfolding distributions which is correlated to the Bragg peak and to estimate the resolution on the fall-off.

To assess the uncertainty on the Bragg peak achievable in a realistic scenario when applying the unfolding, I simulated the interaction of proton beams at 110, 130, 150, 160, 170, 190 MeV impinging a PMMA target, using the same geometry described in subsection 4.1.1. The statistics of primary particles simulated is  $10^{11}$  protons.

The obtained reconstructed spectra has been unfolded using the aforementioned procedure, and the obtained photon profiles are shown in figure Figure 5.19. Plots of the reconstructed photon profile and of the photon profile at production are superimposed. The bias effect seems to be corrected as the unfolding spectrum appears to be in agreement with the true one except for the presence of a smearing effect. This effect is due to statistical uncertainty related to matrix elements of the unfolding procedure.

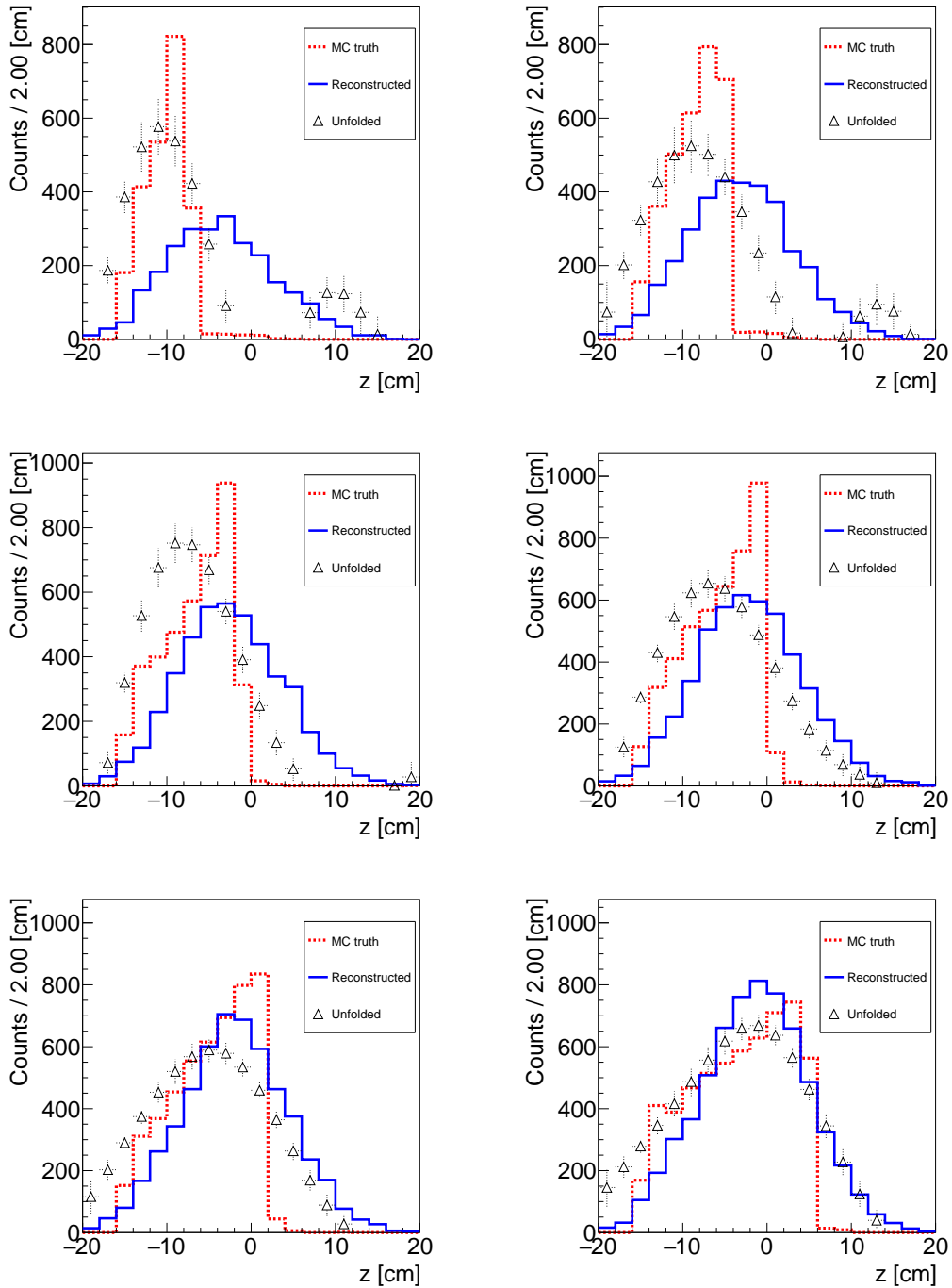


**Figure 5.19.** Reconstructed PG profiles for different proton energy (in order, top to bottom from left to right: 110 MeV, 130 MeV, 150 MeV, 160 MeV, 170 MeV, 190 MeV.), PG profile at pair production and unfolding spectrum are superimposed.

Then a fit on the unfolding fall-off was made using a Fermi-Dirac equation, as in Equation 5.12.

$$f(x) = p_0 \cdot \frac{1}{1 + e^{\frac{z-p_1}{p_2}}} \quad (5.12)$$

where  $p_0$  represents the normalisation parameter,  $p_1$  is the z coordinate of the fall-off of the distribution at the 50% of its maximum and  $p_2$  is the slope of the falling edge of the curve.

The fall-off at 50% is inferred which is related to the Bragg peak, as shown in the plots in Figure 5.19. In Figure 5.20 the fall-off fit of the unfolding spectra for different proton energies are shown.

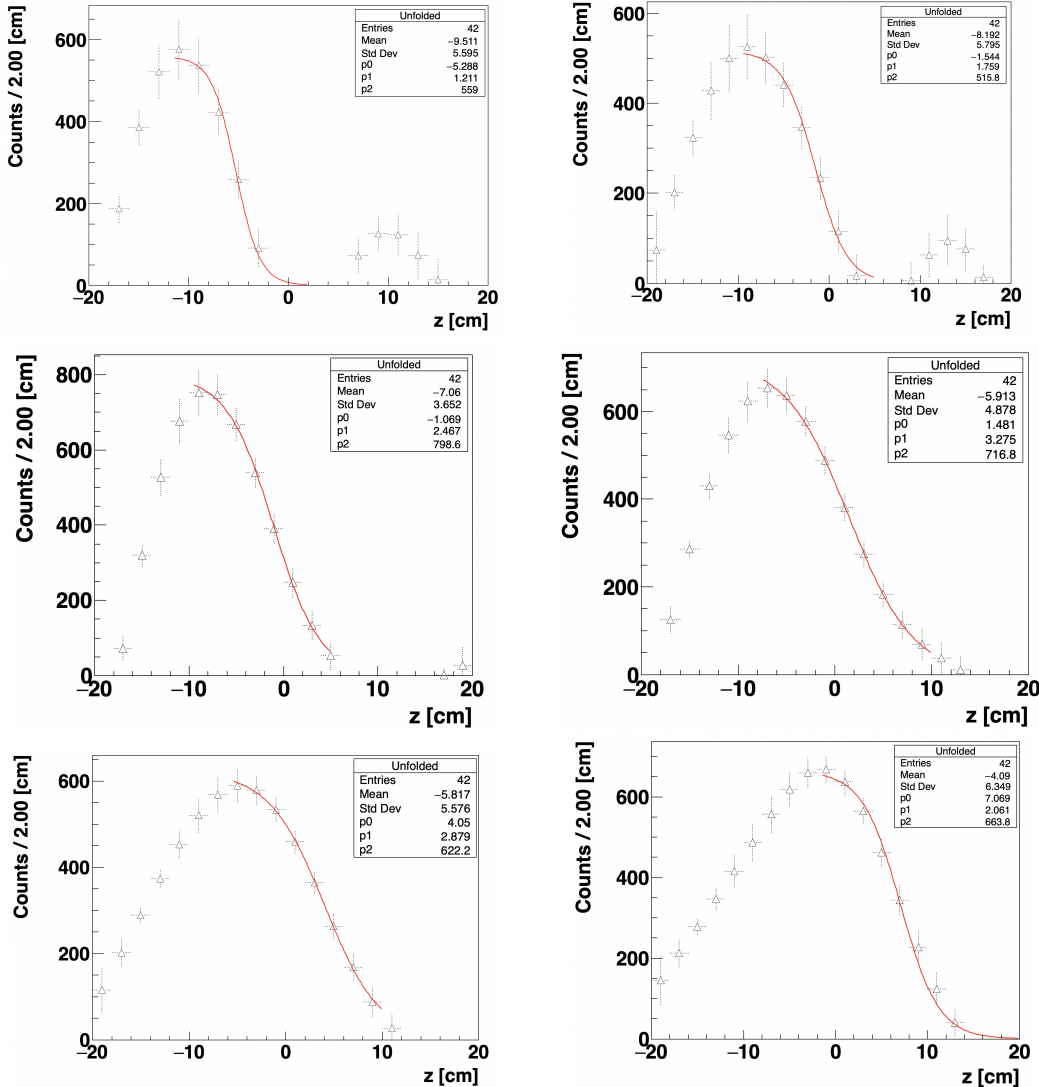


**Figure 5.20.** Unfolding spectra fall-off fit for different proton energy (in order, top to bottom from left to right: 110MeV, 130 MeV, 150 MeV, 160 MeV, 170 MeV, 190 MeV.).

Figure 5.21 shows a plot of the expected Bragg peak value for protons of different energies in PMMA as a function of the corresponding fall-off at 50%.

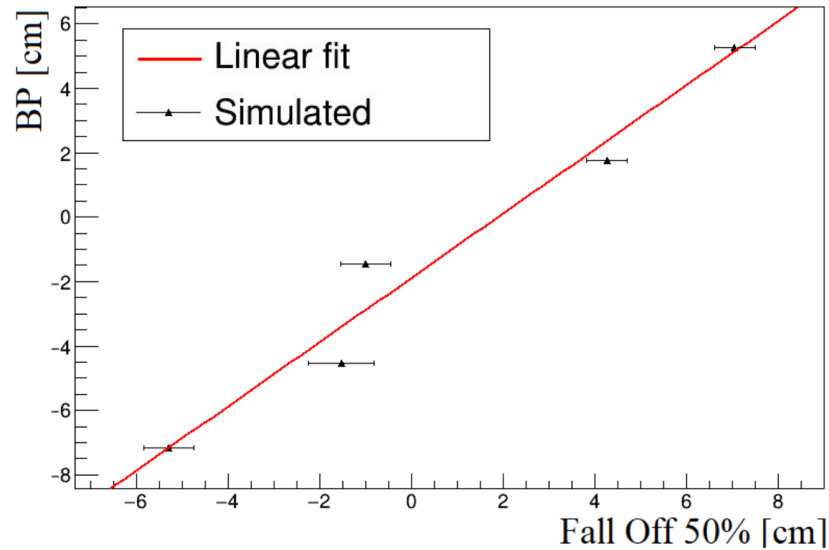


**Figure 5.21.** Expected Bragg peak as a function of the fall-off at 50% considering proton energy of 110MeV, 130 MeV,150 MeV,170 MeV,190 MeV.

A calibration of the theoretical Bragg peak positions as a function of the fall-off at 50% of the unfolded spectra has been performed and the results are shown in Table 5.1. The fit was done by excluding the 160 MeV point, which was then used to compare the expected Bragg Peak.

slope	$1.00 \pm 0.05$ cm
intercept	$-1.89 \pm 0.25$ cm
interpolated BP for 160 MeV protons	$0.64 \pm 0.88$ cm
expected BP for 160MeV protons	$0.05 \pm 0.03$ cm

**Table 5.1.** Fall-off fit results compared with the expected Bragg peak value for 160MeV protons.

The profiles studied have a number of reconstructed photons which depends on the energy and varies from 3000 to 5000 approximately. As mentioned it is reasonable to obtain a number of  $\approx 1000$  tracks reconstructed if the detector acceptance were increased to 2sr. Therefore if the number of tracks considering protons of 160 MeV were re-scaled to 1000 tracks, the resolution would be  $\approx 1$  cm. From Table 5.1 it can be seen that the interpolated BP is compatible within one standard deviation with the expected one. Although the resolution on the fall-off is of  $\approx 1$ cm and the accuracy required in measuring the primary beam range in particle therapy treatments is of the order of  $\approx$  mm. This results are still far from the clinical requirements, and other studies need to be done to optimize the procedure (binning, impact of the matrix uncertainty, regularization). The one presented so far is only a preliminary unfolding study, further studies are foreseen on this topic, but are not being covered by this thesis.

# Conclusions

The PAPRICA (PAir PRoduction Imaging ChAmber) project, funded by the Istituto Nazionale di Fisica Nucleare (INFN), proposes an innovative method for prompt-gamma detection in the context of range monitoring application in particle therapy. The system aims to reconstruct the prompt-gamma emission points, exploiting the photon pair production mechanism. The detection of the two generated leptons (electron and positron) allows to reconstruct the direction of the incident photon and, subsequently, the spatial distribution of the emitted prompt-gamma, which is correlated to the beam range in the patient.

The PAPRICA detector consists of a converter, where the pair production takes place, a tracker, composed by three planes that reconstruct the production vertex of the pair, and a calorimeter, to measure the leptons kinetic energy.

This thesis presents a feasibility study of the PAPRICA chamber, using Monte Carlo simulations developed with FLUKA code.

In my thesis work, I firstly evaluated the more effective strategy to be adopted for triggering and for event selection in a realistic scenario. For this purpose, I studied the energy released in the PAPRICA detector simulating a proton beam of 160 MeV impinging a PMMA phantom. Despite a good detection efficiency could be reached (70-80%) by using a time coincidence between the converter and the calorimeter signal, the high background level, mainly due to prompt-gamma undergoing to Compton interaction ( $\approx 5\%$ ) and secondary protons ( $\approx 89\%$ ), results in a trigger purity of the order of  $10^{-4}$ . Considering a detector dead-time of the order of  $100 \mu s$ , it results in a very low rate of acquired events ( $\sim 1$  Hz). For this reason I pointed out the necessity to develop a second-level trigger capable of a more pure selection. This could be done exploiting the FPGA embedded in the read-out system. Thus, I studied the expected performance of trigger which consider the total energy release and occupancy of the calorimeter and the converter. Selecting the energy in the range  $100\text{keV} < E_{conv} \leq 4\text{MeV}$  and  $E_{calo} \leq 10\text{MeV}$  the contribution of secondary protons is strongly reduced ( $\approx 0.5\%$ ), as well as using a calorimeter occupancy more than 2 pixels, the background due to Compton events is lowered of a factor  $\approx 50\%$ . The efficiency is kept in the range (70-80 %) using threshold  $100E_{conv} \leq 4\text{MeV}$  and  $E_{calo} \leq 10\text{MeV}$  and 2 pixel on with an energy threshold per pixel of 500keV. Instead the the purity improves from the order of  $10^{-4}$  to  $10^{-2}$ .

The possibility to use a passive converter was also studied. The converter material may have an impact on the spatial resolution, as it affect the nuclear recoil and multiple scattering suffered by electrons produced in the detector volume. In this case the trigger was developed using only the calorimeter information. It was set a trigger considering at least 2 activated pixels with a threshold  $E_{thr} = 500\text{keV}$  and an energy threshold  $E_{calo} \leq 10\text{MeV}$ . The efficiency is  $\approx 80\%$  and the purity of the order of  $10^{-3}$ . The background is mainly due to the events that interact by Compton effect in the calorimeter ( $\approx 48\%$ ).

In the second part of my thesis work the reconstruction algorithm used to reconstruct the incoming gamma production point is presented showing the expected spatial resolution in a realistic case. I obtained a spatial resolution of the order of 6 cm, which is completely dominated by the nuclear recoil neglected and the MS suffered by the  $e^+ e^-$  pair exiting from the converter layer. I also found that the spatial resolution is not affected by the lepton energy resolution. However, a systematic effect is observed due to geometrical reasons. To evaluate the range monitoring capability, such effect has to be corrected unfolding the obtained distributions. I carried out a first preliminary study unfolding the photon reconstructed spectra. The bias effect seems to be corrected as the unfolding spectrum appears to be in agreement with the true one except for the presence of a smearing effect. The interpolated Bragg Peak from the unfolding spectrum for 160 MeV protons on PMMA was found  $0.64 \pm 0.88$ , which was compatible within one standard deviation with the expected Bragg peak value. Although the resolution of  $\approx 1\text{cm}$  is not in agreement with the accuracy required in PT (order of mm).

The work carried out in this thesis represents the first feasibility study of the PAPRICA project, which will be continued for the next year.

# Bibliography

- [1] Stewart. "World Cancer Report 2014. International Agency for Research on Cancer". In: 3 (2014).
- [2] R. Wilson. " Radiological use of fast protons" . In: *Radiology* 47 (1946), pp. 487–491.
- [3] U.Amaldi. "History of hadrontherapy". In: *Modern Physics Letters A* Vol. 30, No. 17 (2015).
- [4] PTCOG. *Particle therapy facilities in clinical operation*. 2020. url: <https://www.ptcog.ch/index.php/facilities-in-operation>.
- [5] Particle Data Group. *Passage of particles through matter*. 2013.
- [6] Leo. *Techniques for nuclear and particle physics experiments: a how-to approach*. Springer Science & Business Media, 2012.
- [7] E. Fokas et al., "Ion beam radiobiology and cancer: Time to update ourselves". In:*Biochimica et Biophysica Acta (BBA) - Reviews on Cancer* vol. 1796, no. 2, pp. 216–229, 2009.
- [8] Dieter Schardt, Thilo Elsässer, and Daniela Schulz-Ertner, "Heavy-ion tumor therapy: Physical and radiobiological benefits". In: *Rev. Mod. Phys.* 82, 383 (2010).
- [9] Daniel Cussol, "Nuclear Physics and Hadrontherapy", LPC Caen, ENSICAEN, Université de Caen Basse-Normandie, IN2P3/CNRS.
- [10] Terasawa et al. "Systematic review: charged-particle radiation therapy for cancer". In: *Annals of internal medicine* 151.8 (2009).
- [11] Raju. "Proton radiobiology, radiosurgery and radiotherapy". In: *International journal of radiation biology* 67.3 (1995).
- [12] U. Amaldi, "Radiation Physics: Photons and Charged Hadrons", 2001.
- [13] Durante M. Tommasino F. "Proton radiobiology". In: *Cancers* 7 (2015), pp. 353–381.
- [14] Schwarz. "Treatment planning in proton therapy". In: *The European Physical Journal Plus* 126.7 (2011).
- [15] Uwe Schneider et al. "The calibration of CT Hounsfield units for radiotherapy treatment planning". In:*Phys. Med. Biol.* 41 (1996) 111–124.

- [16] G.Pausch et al. "Detection systems for range monitoring in proton therapy: Needs and challenges". In: *Nuclear Instruments and Methods in Physics Research A* 954 (2018).
- [17] H. Paganetti. "Range uncertainties in proton therapy and the role of Monte Carlo simulations". In: *Physics in Medicine & Biology* 57.11 (2012).
- [18] K. Parodi. "PET monitoring of hadrontherapy". In: *Nuclear Medicine Review* 15.C (2012), pp. 37–42.
- [19] K. Parodi. "On-and off-line monitoring of ion beam treatment". In: *Nuclear Instruments and Methods in Physics Research Section A* 809 (2016).
- [20] Ferrero V. et al. "The INSIDE project: on-line monitoring and simulation validation with the in-beam PET scanner". In: *Journal of Physics: Conference Series* 841 (2017).
- [21] K.Parodi et al. "Patient study on in-vivo verification of beam delivery and range using PET/CT imaging after proton therapy". In: *Int J Radiat Oncol Biol Phys* 68 (2007), pp. 920–934.
- [22] Hishikawa Y. et al. "Usefulness of positron-emission tomographic images after proton therapy". In: *J Radiat Oncol Biol Phys* 53 (2002), pp. 1388–1391.
- [23] Zhu X. et al. "Monitoring proton radiation therapy with in-room PET imaging". In: *Phys Med Biol* 56 (2011), pp. 4041–4057.
- [24] Agodi C. et al. "Charged particle's flux measurement from PMMS irradiated by 80 Mev/u carbon ion beam". In: *Physics in Medicine and Biology* 57(18) (2012), p. 5667.
- [25] L. Piersanti et al. "Measurement of charged particle yields from PMMA irradiated by a 220 MeV/u C12 beam". In: *Physics in Medicine and Biology* 59 (2014), pp. 1857–1872.
- [26] Gwosch et al. "Non-invasive monitoring of therapeutic carbon ion beams in a homogeneous phantom by tracking of secondary ions". In: *Physics in Medicine & Biology* 58.11 (2013).
- [27] Muraro et al. "Monitoring of hadrontherapy treatments by means of charged particle detection". In: *Frontiers in oncology* 6 (2016).
- [28] Krimmer et al. "Prompt-gamma monitoring in hadrontherapy: A review". In: *Nuclear Instruments and Methods in Physics Research Section A* 878 (2018).
- [29] Pinto et al. "Absolute prompt-gamma yield measurements for ion beam therapy monitoring". In: *Physics in Medicine & Biology* 60.2 (2014).
- [30] Verburg et al. "Energy-and time-resolved detection of prompt gamma-rays for proton range verification". In: *Physics in Medicine & Biology* 58.20 (2013).
- [31] Min C.H. et al. "Prompt gamma measurements for locating the dose falloff region in the proton therapy". In: *Appl. Phys. Lett.* 89 18 (2006).
- [32] Kin et al. "Pinhole Camera Measurements of Prompt Gamma-rays for Detection of Beam Range Variation in Proton Therapy". In: *Journal of the Korean Physical Society* Vol. 55, No. 4, October 2009, pp. 1673-1676

- [33] Krimmer J . et al. "Collimated prompt gamma TOF measurements with multi-slit multi-detector configuration". In: *J. Instrum.* 10 1 (2015).
- [34] Smeets et al. "Prompt gamma imaging with a slit camera for real-time range control in proton therapy". In: *Physics in Medicine & Biology* 57.11 (2012).
- [35] Park et al. "Comparison of knife-edge and multi-slit camera for proton beam range verification by Monte Carlo simulation". In: *Nuclear Engineering and Technology* 51.2 (2019).
- [36] Fernando Hueso-González et al. "Compton Camera and Prompt Gamma Ray Timing: Two Methods for In Vivo Range Assessment in Proton Therapy". In: *Front. Oncol.* 6 (2016).
- [37] Thirolf et al. "Development of a Compton camera for online range monitoring of laser-accelerated proton beams via prompt-gamma detection". In: *vol. 66. EDP Sciences*. 2014.
- [38] Werner et al. "Processing of prompt gamma-ray timing data for proton range measurements at a clinical beam delivery". In: *Physics in Medicine & Biology* 64.10 (2019).
- [39] Hueso-Gonz et al. "A full-scale clinical prototype for proton range verification using prompt gamma-ray spectroscopy". In: *Physics in Medicine & Biology* 63.18 (2018).
- [40] Krimmer et al. "A cost-effective monitoring technique in particle therapy via uncollimated prompt gamma peak integration". In: *Applied Physics Letters* 110.15 (2017).
- [41] Kanbach et al. "The project EGRET (energetic gamma-ray experiment telescope) on NASA's Gamma-Ray Observatory GRO". In: *Space Science Reviews* 49.1-2 (1989).
- [42] Wu et al. "PANGU (PAir-productioN Gamma-ray Unit): A High Resolution Gamma-ray Space Telescope)". In: *PoS* (2015).
- [43] H. Rohling et al. "Simulation Study of a Combined Pair Production – Compton Camera for In-Vivo Dosimetry During Therapeutic Proton Irradiation". In: *IEEE TRANSACTIONS ON NUCLEAR SCIENCE VOL. 62, NO. 5, OCTOBER 2015*
- [44] Motz et al. "Pair production by photons". In: *Reviews of Modern Physics* 41.4 (1969).
- [45] W-M Yao et al. "Review of Particle Physics". In *J. Phys. G: Nucl. Part. Phys.* 33 1 (2006).
- [46] Salvat et al. "PENELOPE-2006: A code system for Monte Carlo simulation of electron and photon transport". In: *Workshop proceedings*. Vol. 4. 6222. 2006.
- [47] Glenn F Knoll. *Radiation detection and measurement*. John Wiley & Sons, 2010.
- [48] Rinella et al. "The ALPIDE pixel sensor chip for the upgrade of the ALICE Inner Tracking System". In: *Nuclear Instruments and Methods in Physics Research Section A: Accelerators, Spectrometers, Detectors and Associated Equipment* 845 (2017).

- [49] Traini et al. “Review and performance of the Dose Profiler, a particle therapy treatments online monitor”. In: *Physica Medica* 65 (2019).
- [50] Ciciriello F. et al. “BASIC32-ADC, a Front-end ASIC for SiPM Detectors”. In: *Nuclear Science Symposium and Medical Imaging Conference* (NSS/MIC), IEEE (2013), pp. 1–6.
- [51] Ferrari et al. “FLUKA: a multi-particle transport code CERN-2005-10”. In: *INFN/TC* 5 (2005).
- [52] Battistoni et al. “The FLUKA code: an accurate simulation tool for particle therapy”. In: *Frontiers in oncology* 6 (2016).
- [53] Mattei et al. “Scintillating Fiber Devices for Particle Therapy Applications”. In: *IEEE Transactions on Nuclear Science* 65.8 (2018)